UNIVERSITY OF OKLAHOMA

GRADUATE COLLEGE

RAWINSONDE OBSERVATIONS OF SUPERCELL-ENVIRONMENT INTERACTIONS

A THESIS

SUBMITTED TO THE GRADUATE FACULTY

in partial fulfillment of the requirements for the

Degree of

MASTER OF SCIENCE IN METEOROLOGY

By

ANDREW WADE
Norman, Oklahoma
2016

RAWINSONDE OBSERVATIONS OF SUPERCELL-ENVIRONMENT INTERACTIONS

A THESIS APPROVED FOR THE
SCHOOL OF METEOROLOGY

BY

____
Dr. Michael Biggerstaff, Chair

____
Dr. Michael Coniglio, Co-Chair

____
Dr. Michael Richman

Table of Contents

List of Figures

Abstract

The Mesoscale Predictability Experiment (MPEX) in 2013 and Mini-MPEX in 2016 used mobile soundings to observe the near-storm environments of springtime Great Plains convection. Together, the projects collected over 100 soundings in supercell inflow environments. To explore possible storm-induced changes to the inflow environment, close-range soundings in the near inflow of supercells were compared to near-simultaneous background soundings released farther away. Several VORTEX2 soundings supplement the MPEX/Mini-MPEX dataset, resulting in 28 near-far inflow pairs from a wide variety of tornadic and nontornadic supercells. Composite soundings were created for the near- and far-field subsets, as well as tornadic and nontornadic subsets.

A brief synopsis of Mini-MPEX upsonde operations is presented. Low-level thermodynamic and kinematic variables in the near and distant inflow are compared. Composite skew-Ts and hodographs are used to illuminate differences between near and far inflow soundings, as well as between tornadic and nontornadic cases, particularly in terms of low-level stability and near-field hodograph enhancement. Finally, unique observations from individual MPEX and Mini-MPEX cases are discussed in the context of the near-field/far-field comparison.

1. Introduction

Supercells, convective storms with persistent rotating updrafts (AMS 2012), are prolific producers of severe weather compared to other storm modes (e.g., Nelson 1976) and are responsible for a disproportionate share of tornadoes and large hail in the United States (Smith et al. 2012). Because supercells pose such well-established hazards to life and property, they were of interest to two related field experiments, the Mesoscale Predictability Experiment (MPEX; Weisman et al. 2015) in 2013 and Mini-MPEX in 2016. This thesis is an analysis of MPEX and Mini-MPEX mobile sounding data (Trapp et al. 2016) aimed at improving understanding of the near-storm environment and supercells' interactions with it. More narrowly, soundings observed very near supercells are compared to background environmental profiles to isolate storm effects; a series of relevant cases from MPEX and Mini-MPEX are then discussed in the context of the near-storm environment.

a. Early supercell research

Focused supercell research began when analyses of severe storms near Wokingham, England (Browning and Ludlam 1962) and Geary, Oklahoma (Browning and Donaldson 1963) revealed strikingly similar structures in radar reflectivity. These included a "forward overhang," an "echo-free vault" marking a persistent strong updraft, and a "wall." Browning and Donaldson (1963) noted the pattern and inferred an "important class of local storms…developing within a strongly sheared environment which remain persistently intense and tend toward a steady state circulation." Browning's (1964) radar study of severe local storms was the first publication to use the word ‘supercell’: “[S]ingle large cells (supercells) with characteristic structures…were maintained in a more or less steady state as the storms traveled to the right of the winds for periods of several hours.” The same study noted continuous, rather than discrete, propagation of supercells and proposed a simple three-dimensional model of flow in severe right-moving storms.

Knowledge of supercells expanded with a proposed life cycle and three-dimensional conceptual model by Lemon and Doswell (1979), as well as the discovery that tilting of ambient horizontal vorticity into the vertical by the updraft was the predominant source of supercell rotation (Barnes 1970, Rotunno 1981, Davies-Jones 1984, Rotunno and Klemp 1985). Analysis of storm-induced pressure perturbations found that nonlinear effects were responsible for storm splitting, while linear effects favored right-moving supercells when hodographs curved clockwise (Rotunno and Klemp 1982). Baroclinic generation of vorticity along gust fronts at the edges of downdrafts was determined to be important for low-level mesocyclogenesis (Rotunno and Klemp 1985).

b. Review of supercell environments

The importance of the ambient state of the atmosphere to the intensity and organization of deep convection was known even before supercell structures were identified; Beebe’s (1956) composite synoptic-scale environments of tornadoes featured winds increasing and veering with height, southerly surface flow, and moisture ridges. Whiting and Bailey (1957) also connected tornadoes with high-dewpoint environments, and Dessens (1960) associated severe hailstorms with strong upper flow. But as more was discovered about the structure and dynamics of supercells, recent studies of storms' mesoscale environments more thoroughly identified necessary ingredients for supercells and associated tornadoes. Hart and Korotky (1991) formulated the energy-helicity index (EHI), the product of convective available potential energy (CAPE) and storm-relative helicity (SRH), for use in identifying severe weather environments. Rasmussen and Blanchard (1998) found EHI to be skillful in distinguishing significant tornado environments from others, and also suggested that low lifted condensation level (LCL) heights favored significant tornadoes. Thompson et al. (2002) combined several known severe weather ingredients into the significant tornado parameter (STP) and supercell composite parameter (SCP). Rasmussen (2003) recommended calculating SRH in the layer extending to 1 km above ground level (AGL) for discriminating between tornadic and nontornadic supercells, instead of a deeper layer; Markowski et al. (2003) arrived at a similar conclusion using Rapid Update Cycle (RUC) wind profiles. Thompson et al. (2003), also using RUC analyses, noted the utility of 0-1-km SRH, mixed-layer LCL height, and SCP and STP for the same purpose. Craven and Brooks (2004) found low-level shear and LCL height most useful for separating significant tornado soundings from others. Thompson et al. (2007) and Thompson et al. (2012) revisited analyses of supercell and tornado environments with the effective inflow layer (a layer where parcels have positive CAPE and relatively small CIN) and with respect to season and convective mode. This is only a small sample of the publications attempting to describe characteristics of severe weather environments, but gives a sense of the relevant parameters: CAPE, shear, and 0-1-km SRH, with LCL heights also important if considering tornado production.

c. Storm-environment interactions

The copious literature on supercell and tornado environments is mostly devoted to the environment's effects on the storm. Comparatively little has been written about the reverse. The first inquiry in this area may have been Fankhauser's (1971) observations of flow around an intense convective cell with airborne Doppler radar and chaff. The study likened midlevel flow around a storm to flow around a stationary rotating cylinder with diffluence upstream and confluence downstream, but also noted entrainment of chaff in the storm itself. This indicated some turbulent mixing around the edges of the storm, suggesting subsequent evaporative cooling of midlevel environmental air as an origin of downdrafts. From these observations, a rough three-dimensional model of flow in and around a persistent updraft was formulated.

In soundings from a National Severe Storms Laboratory rawinsonde network in Oklahoma, Barnes (1978) noted subtler influences of a supercell on the environment downstream of the updraft: there was evidence of unsaturated ascent suggesting a midlevel vertical circulation in front of the updraft, as well as boundary layer subsidence. [Trapp et al. (2016) briefly described comparable observations during MPEX.] Lilly (1986a) composed a kinetic energy cycle for supercells containing a loop in which mean flow kinetic energy (a source) is transferred to a storm's rotational kinetic energy, which is transferred to the storm's divergent kinetic energy, which in turn is transferred back to mean flow kinetic energy. This implies that a storm's modification of the ambient environment could ultimately affect the storm itself.

More recently, Brooks et al. (1994b) noted an example of helicity spiking at a vertical wind profiler site just before the passage of a nearby mesocyclone, but also provided an example of a similar event with no clear rise in helicity, illustrating the difficulty of observing consistent storm-induced environmental changes. Markowski et al. (1998a) demonstrated that low-level cooling from anvil shading in three observed supercells was sufficient to contribute baroclinically generated vorticity to inflow parcels passing along the edges of anvil shadows. Because of mixing associated with strong low-level shear, the cooling was shown to result in a shallow, weakly stable layer instead of a pronounced inversion under the anvil.

Potvin et al. (2010), in determining an appropriate spatiotemporal range for proximity soundings representing tornado environments, accounted for storms' effects on their environments. Soundings within 40 km of a tornado's eventual location most consistently represented a favorable tornado environment when taken 1-2 h before the tornado, and it was recommended that soundings 0-1 h before a tornado be 40-80 km removed from the tornado. This implies that within 40 km of the tornado-producing region of an ongoing supercell, the environment may be substantially modified by the storm.

Parker (2014) investigated supercells' interactions with the background environment using a composite environment created with observed soundings from various locations around supercells. This work incorporated 134 soundings from 7 tornadic supercells and 5 nontornadic supercells; the Second Verification of the Origins of Rotation in Tornadoes Experiment (VORTEX2; Wurman et al. 2012) made such dense sampling possible. In general, the near inflow appeared more favorable for supercells and tornadoes than the far inflow. With decreasing distance to the storm, the boundary layer cooled and moistened and low-level shear increased. Tornadic storms' inflow had higher STP and SCP than that of nontornadic storms. Nontornadic storms had drier boundary layers and less low-level shear in the distant inflow; storm-induced changes to the wind field brought low-level shear closer to that of tornadic storms in the near inflow, but much of the associated horizontal vorticity was crosswise rather than streamwise. Simulations by Nowotarski and Markowski (2016) agreed that supercells increase low-level shear, and the effect was greater when anvil shading was included. Anvil shading also decreased boundary layer buoyancy, weakening buoyancy gradients at a storm's outflow boundaries.

With relatively few publications describing supercells' influences on their immediate environments, and even fewer investigating the storms' effects on their inflow, this is chosen as the primary avenue for analysis of MPEX and Mini-MPEX soundings herein.

2. Data and methods

a. The Mesoscale Predictability Experiment

MPEX investigated the possibility of improving short-term predictability of deep convection and its upscale effects with targeted mesoscale observations. The field phase was conducted in spring 2013 with mobile sounding vehicles from the National Severe Storms Laboratory (NSSL), Colorado State University (CSU), Purdue University (PU), and Texas A&M University (TAMU). All units used InterMet radiosonde systems except for CSU (which used Vaisala), and all units used helium-filled 200-g latex balloons to carry the radiosondes. Details of MPEX upsonde operations may be found in Trapp et al. (2016). MPEX contributed 54 supercell inflow soundings to this dataset (criteria used to define inflow soundings are given in Section 2f).

b. Mini-MPEX

Mini-MPEX in spring 2016 used two NSSL mobile sounding vehicles and the newly built Collaborative Lower Atmospheric Mobile Profiling System 2 (CLAMPS-2) to add substantially to the dataset of supercell inflow soundings obtained from MPEX. Containing a Doppler lidar, the Atmospheric Emitted Radiance Interferometer (AERI), and a microwave radiometer, CLAMPS-2 focused on boundary-layer observations, but was also equipped to contribute pre-convective and far-field soundings. All units used Vaisala RS-92 radiosondes and helium-filled 200-g latex balloons.

Mini-MPEX's mission was twofold. Leading up to convective initiation, radiosonde and profiler observations of the pre-storm environment were collected for assimilation into convection-allowing models. Once storms initiated and became supercellular, additional sondes were launched in the near and far inflow, sampling both simultaneously where possible. NSSL mobile sounding vehicles obtained these storm-following inflow soundings, as CLAMPS-2 had limited mobility and could not operate in precipitation. This resulted in a set of 52 supercell inflow soundings from 10 severe weather days. The combined MPEX/Mini-MPEX dataset contained 106 supercell inflow soundings. Their release points are plotted in a storm-relative sense in Fig. 1.

c. Quality control

The raw 1 Hz data were plotted and manually examined for obvious errors in temperature, humidity, pressure, and wind. Any data point with a higher pressure than the previous valid data point was removed, eliminating both vertical oscillations due to storm-scale downdrafts and the rapid descent of the sonde after balloon rupture. Some levels had valid data for certain variables and invalid/missing data for others; in such cases, interpolation (linear on a log-*p* scale) was used to complete the profile. To remove the pendulum motion of the radiosonde beneath the balloon, which appears as a regular ~15-s period of oscillation in GPS-derived wind data, a triangular filter with a full width of 67 data points (chosen by experimentation and manual inspection of hodographs) was used. The filter width became progressively smaller as needed toward the ends of the profile.

Each NSSL sounding van was equipped with a mobile mesonet unit (e.g., Straka et al. 1996) recording atmospheric pressure, temperature, relative humidity, and wind speed and direction at one-second intervals. Crews in the field input wind data from the mobile mesonet unit as the surface wind in the GPS Advanced Upper-Air Sounding System (GAUS) program. Surface values of temperature, pressure, and relative humidity were transferred directly from the radiosonde to GAUS. To minimize exposure errors, the radiosonde was kept out of direct sunlight as long as possible and was then placed on a portable wooden box or manually held off the ground by its string during this part of the prelaunch routine, as far as reasonably possible from the van and from paved surfaces. Crews were able to compare sonde data to mobile mesonet data in real time.

d. Calculation of sounding variables

Original code was written for calculation of sounding variables. Surface-based parcels were assigned the temperature and relative humidity recorded at the surface. A layer extending to 100 hPa above ground level (AGL) was used for mixed-layer parcels. The parcel was lifted at the dry adiabatic lapse rate from the surface until its mixing ratio reached the saturation mixing ratio it had at the surface. At that LCL, the parcel's equivalent potential temperature was calculated according to Bolton's (1980) recommended formulation. At each level above, the parcel temperature was decremented by 0.01 K until the original equivalent potential temperature was reached, since equivalent potential temperature is conserved for the lifted parcel. This introduced considerably less error than calculating a moist adiabatic lapse rate at each level and lifting the parcel at that rate to the next level. The virtual temperature correction was used in calculating CAPE and CIN (Doswell and Rasmussen 1994).

For determining storm-relative helicity, observed storm motion was desired, both for accuracy and because soundings often did not reach the 6 km AGL required for calculating Bunkers supercell motion (Bunkers et al. 2000). The center of the mesocyclone was manually located using the nearest WSR-88D, at the lowest tilt of the scan nearest to launch time. It was located again one hour later. The range and bearing from the first to the second were used to define the observed storm motion over the hour following launch.

e. Reliability of RAP background soundings

In total, MPEX and Mini-MPEX obtained 106 supercell inflow soundings. Ideally, each would be compared to some base state or background environment entirely uninfluenced by the storm. However, the limited number of sounding units on these projects meant that such environmental soundings were not intentionally obtained while storms were in progress; those that were taken did not often coincide temporally with a nearer sounding for comparison. One prospective solution was to use Rapid Refresh (RAP) model analysis "soundings" as the background or far-field profiles, since profiles from its predecessor, the RUC, were often used in storm environment studies (e.g., Rasmussen and Blanchard 1998, Thompson et al. 2003). To determine whether RAP profiles could safely be used in this way, it was necessary to test them for biases in similar scenarios—warm-season, mostly diurnal, convectively unstable Great Plains environments.

102 environmental soundings from MPEX were compiled. These were selected so that the soundings could not possibly have been contaminated by deep moist convection. Some were from days where storms were expected but did not form nearby. Others were launched before convective initiation. Still others were in inflow, but were more than 80 km away from any robust storm and remained uncontaminated. RAP analyses were obtained at the nearest hour for these cases, and vertical profiles were created at the grid point nearest the sounding release site. To avoid making assumptions about the unknown distribution of RAP errors, bootstrapping—rather than a *t* test or some similar method—was chosen for statistical assessment of RAP biases. Using the R ‘boot’ package, confidence intervals for RAP biases in several relevant variables were bootstrapped with 5000 replicates.

The only statistically significant biases were all directly related to a known warm and dry bias at the surface (Weygandt et al. 2015). With 95% confidence, the warm bias in surface temperature was 1.17 K to 2.09 K and the dry bias in surface dewpoint temperature was 0.83 K to 2.50 K. In subsequent sections, it will become clear that these errors are of the same magnitude as typical storm-induced changes to supercell inflow. These errors were present during spring 2016 Mini-MPEX operations as well, since the implementation of the RAP that reduced these biases became operational in October 2016. This precludes using RAP profiles as a base state for comparison to observed near-storm soundings. However, successfully replicating the subtle but consistent warm and dry bias of the RAP validates the use of rawinsonde observations to investigate small changes in the near-storm boundary layer.

f. Near-far inflow pair selection

The unsuitability of RAP background profiles necessitated restricting the dataset to roughly simultaneous pairs of observed soundings, one in the near inflow and one in the distant inflow. Potvin et al. (2010) defined a “Goldilocks zone” for proximity soundings for severe weather events. Soundings most representative of the mesoscale environment are found at a range of 0-40 km from the storm 1-2 hours before a severe weather event, or 40-80 km up to one hour before the event. This implies that any effects of an ongoing storm on its inflow are usually found within 40 km of the storm, while the area more than 40 km distant is uncontaminated and representative of the background environment. Therefore, in this study, near-field inflow soundings were defined as those within 40 km of an ongoing supercell. For each near-field sounding, a matching far-field sounding was sought. To constitute a valid near-far pair, the distant sounding must have been launched at least 10 km farther afield than the near sounding, and the two must have been released within 30 minutes of each other. This usually resulted in the far-field half of the pair meeting the Potvin et al. (2010) criteria for a proximity sounding.

These criteria produced a set of 19 near-far pairs from MPEX and Mini-MPEX. These were supplemented with 9 pairs from VORTEX2 for a total of 28 near-far pairs. 12 pairs designated as ‘tornadic’ were from storms that were producing tornadoes at launch time or did so within one hour after launch, as verified by spotter reports and the Storm Prediction Center storm report database. 16 pairs not meeting that criterion were designated 'nontornadic.' The 12 tornadic pairs were drawn from 9 tornadic supercells, and the 16 nontornadic pairs were drawn from 10 nontornadic supercells. Four supercells were sampled as both tornadic and nontornadic in different phases of their evolution. While these sample sizes are somewhat small, the Parker (2014) composite supercell environments were created using observations from only 7 tornadic supercells and 5 nontornadic supercells. Since observed soundings within 40 km of tornadic supercells with near-simultaneous far-field soundings for comparison do not occur unless specifically sought in field research, this is the largest such dataset that currently exists to the author's knowledge. Future work in this area would benefit from further mobile sounding operations in the mold of Mini-MPEX.

Several additional notes on the dataset are in order. First, the sampling strategies for distant inflow soundings differed from VORTEX2 to MPEX/Mini-MPEX. VORTEX2 crews tended to release soundings close to the path of the storm, while MPEX/Mini-MPEX far-field soundings were farther to the right of the storm's path. The difference is noted in Fig. 2, which shows the storm-relative location of each pair. Second, there is no meaningful difference between the ranges of tornadic and nontornadic near-field soundings (means of 26.5 and 25.4 km from the storm, respectively). Third, the tornadic sounding pairs were launched at 2046 UTC on average, while nontornadic pairs averaged 2332 UTC. This is one example of how such work would benefit from a larger sample size. Impacts of the discrepancy between tornadic and nontornadic pairs' mean launch times are discussed in following sections. Fourth, the mean near-field range (26 km from the storm) and far-field range (56 km) are both nearer than the points selected from the composite analyses of VORTEX2 soundings in Parker (2014) to represent the near and far inflow, which were 40 and 80 km from the storm. Finally, the fundamental assumption required for comparing simultaneous near- and far-field soundings is that the two soundings would be roughly identical in the absence of the supercell—that is, that there are no significant preexisting heterogeneities in the sampled environment. Obvious violations of this assumption were avoided. Care was taken to ensure that sounding pairs came from a single airmass, rather than being separated by some mesoscale boundary. As an example, Figs. 3 and 4 depict a sounding pair from 19 May 2010 that was excluded on this basis.

3. Results and discussion

a. All supercell inflow soundings

The combined MPEX/Mini-MPEX dataset contains 58 soundings in the near inflow of supercells (20 tornadic and 38 nontornadic) and 49 distant inflow soundings (22 tornadic and 27 nontornadic). A few relevant parameters are discussed for these subsets. CAPE and deep-layer shear, though necessary for supercells, are generally disregarded throughout this study because many near-storm soundings ended before reaching the altitude needed to compute CAPE and/or deep-layer shear. Fig. 5 shows distributions of mixed-layer CIN (MLCIN) for each subset. The values are in a range to be expected for severe storm environments, but values in far-field tornadic and nontornadic subsets are not as expected. Tornadic environments tend to have less CIN than nontornadic environments in past analyses of near-storm soundings (e.g., Davies 2004, Thompson et al. 2007), but the opposite appears in the present study. Notably, large CIN is not often present in the near inflow of any supercells, tornadic or nontornadic. In Fig. 6, mixed-layer LCL (MLLCL) heights are compared across these subsets. While many nontornadic storms also have low LCLs, it is clear that there is a certain upper limit near 1500 m above which tornado production does not occur in these cases, while many of the nontornadic far-field soundings have higher LCLs. This is consistent with Rasmussen and Blanchard (1998), Thompson et al. (2003), Craven and Brooks (2004), and others. Finally, Fig. 7 compares 0-1-km SRH for the same groups of soundings. As is expected, far-field SRH appears related to tornado production as median 0-1-km SRH is larger for the tornadic soundings, and typical values of 150-500 $m^2 s^{-2}$ for tornadic storms are mostly consistent with existing climatologies.

b. Near-minus-far perturbations

Inconsistent sampling poses problems for the results in the section above; it is well known, for example, that large CIN does not favor tornadoes, yet far-field sampling of one or two high-CIN tornadic cases makes it appear so—Figs. 8 and 9 are examples of high-CIN profiles from the distant inflow of tornadic storms. To avoid such confusion, it is best to compare a near-field sounding to a background sounding farther away to isolate storm-induced changes. The rest of the results section deals exclusively with the 28 pairs of approximately simultaneous soundings in the near and far inflow of supercells, rather than the full set of supercell inflow soundings discussed above. Values of relevant variables in far-field inflow soundings were subtracted from the corresponding near-field values to yield distributions of near-storm perturbations from the background environment. This section describes those results.

i. Surface temperature

Fig. 10 shows distributions of surface temperature perturbations for tornadic sounding pairs, nontornadic pairs, and all pairs combined. All pairs tend to cool somewhat in the near field; warming is seldom observed. Both tornadic and nontornadic sets are centered on very small negative perturbations. However, the interquartile range of nontornadic pairs extends into larger negative perturbations than that of the tornadic pairs.

Surface temperature perturbations must be treated with caution because of the effect of elevation. Nearly all near-field soundings were released farther west and at a higher elevation than the corresponding far-field soundings, such that any inflow parcel passing through both points would experience adiabatic cooling independent of the storm. However, elevation is not the only possible cause of cooler temperatures in the near inflow. Anvil shading can also produce a shallow, cooler, stable layer at the surface (Markowski et al. 1998a, Nowotarski and Markowski 2016).

ii. Surface potential temperature

To remove the effect of upslope adiabatic cooling from the distant inflow to the near inflow, surface potential temperature was calculated for each sounding. Anvil shading or other diabatic effects should appear as changes in potential temperature. The results are in Fig. 11, plotted in the same way as the temperature perturbations. There is considerable variability for all cases, but in the tornadic set, there is often slight diabatic warming from the far inflow to the near inflow and cooling is rare. At the least, there is no evidence of consistent diabatic cooling resulting from anvil shading, particularly with tornadic storms. This apparent contradiction of Markowski et al. (1998a) and Nowotarski and Markowski (2016) may arise in part from differences in the storm-relative locations of inflow soundings. These studies of anvil shading often focused on areas close to the forward-flank gust front and near the path of the storm, where parcels have longer residence times beneath the storm's anvil. While Mini-MPEX sounding crews in the near inflow were nearly always in the anvil's shadow, it is possible that they tended to be closer to the edge of the shadow to the right of the storm's path, where near-surface parcels had not been shaded for very long.

iii. Relative humidity and lifted condensation level

Fig. 12 contains boxplots of changes in surface relative humidity. While distributions for both tornadic and nontornadic subsets appear centered around a slight moistening in the near inflow—consistent with the slight cooling and boundary layer moistening in Parker (2014)—the changes in RH are highly variable and the mean increase is very small. In accordance with minimal cooling and moistening restricted to a layer near the surface, mixed-layer lifted condensation levels (Fig. 13) change very little in the near inflow for tornadic and nontornadic cases.

iv. Convective inhibition

Parker (2014) reported a modest increase in CIN in the near inflow of the composite supercell environment for both tornadic and nontornadic cases. Nowotarski and Markowski (2016) found that anvil shading decreased buoyancy in the boundary layer. However, the sounding pairs in this dataset did not reveal a consistent increase in CIN in the near inflow. Fig. 14 is a set of boxplots of MLCIN perturbations. CIN was treated as negative for these distributions, so a positive value corresponds to less CIN in the near inflow than in the far inflow. Regardless of tornado production, virtually all observed changes in MLCIN in the near inflow were small—less than 20 J kg^{-1} in magnitude. For reference, Fig. 15 displays the actual values of MLCIN in the four subsets of soundings. It should be noted that many cases had negligible MLCIN in the background environment to begin with.

v. Storm-relative helicity and low-level shear

The most consistent finding in examining distributions of near-field perturbations is the enlargement of low-level hodographs by tornadic supercells. Fig. 16 shows distributions of the changes in 0-1-km shear magnitudes; Fig. 17 is similar, except for 0-1-km SRH. Particularly in SRH, there is a distinct difference between tornadic and nontornadic cases: only in the near inflow of tornadic supercells does SRH appear to be consistently enhanced. The difference between mean tornadic and nontornadic perturbations is statistically significant; despite the small samples, bootstrap testing yielded a p-value less than 0.01. (Bootstrap testing on other variables found the differences between tornadic and nontornadic perturbations to be insignificant or too small to be relevant.) This result seems to contradict the Parker (2014) composite environments, in which nontornadic supercells enlarged the low-level hodograph and increased SRH more than tornadic supercells did. However, this could be a result of both the near- and far-field soundings in this dataset being, on average, considerably closer to the storm than the near and far inflow points defined in Parker (2014). Another key difference is that these are individual soundings that drift with the surrounding flow, as opposed to vertical profiles drawn from an objective analysis of the sounding data. This generally results in the sonde drawing even closer to the low-level updraft after release, and presumably experiencing greater accelerations toward the storm.

c. Composite soundings

To characterize the mean storm-induced modifications to a typical inflow environment, composite soundings were created for the near-field tornadic, far-field tornadic, near-field nontornadic, and far-field nontornadic subsets. These composites only extend from the surface to 3 km AGL; this level was chosen because many soundings ended in midlevels with loss of sonde signal, and because of increasing sonde drift with height. For creation of these composites, each observed and quality-controlled sounding was interpolated linearly with respect to height to intervals of 10 m AGL. The high vertical resolution of the quality-controlled data allowed interpolation to these levels with minimal introduction of error. Sounding variables were then averaged at each interval.

In comparing near-field and far-field nontornadic soundings (Fig. 18), two features are noteworthy. First, there is marked cooling and moistening above the boundary layer. Evaporation may be a factor near the top of the composite profiles, since sondes sometimes drifted close to forward-flank precipitation and the far-field profile was very dry above the boundary layer. However, storm-induced lifting would also result in similar cooling and moistening; rough calculations show that with an environmental lapse rate of ~7 K km^{-1}, in the 3000 s required for ~10 m s^{-1} flow to traverse the mean 30 km between soundings, 1 K of cooling may be achieved with only ~0.1 m s^{-1} storm-induced ascent. Second, a very shallow stable layer at the surface, not present in the far inflow, appears in the near inflow. This is consistent with the effects of anvil shading. It is likely not a manifestation of nocturnal cooling, despite the relatively late timing of the nontornadic soundings, because no evidence of a surface inversion appears in the far-field composite. Hodographs were also generated for the composite soundings. The near- and far-field nontornadic hodographs are overlaid in Fig. 19. They are nearly identical.

The near- and far-field tornadic composite soundings are plotted in Fig. 20. Their temperature and moisture profiles are much more similar than the near- and far-field nontornadic composites. There is no evidence of cooling at the surface; in fact, a small *increase* in surface potential temperature from the far inflow to the near inflow is evident, consistent with the near-field perturbations shown in the preceding section (Fig. 11). In contrast to the nontornadic case, the composite hodograph is significantly enlarged in the near inflow (Fig. 21). This demonstrates the increase in 0-1-km SRH near tornadic supercells that is seen in the near-field perturbations (Fig. 17).

Far-field composites for tornadic and nontornadic storms are compared in Fig. 22. This comparison requires caution because of the discrepancy in diurnal timing, with tornadic soundings averaging over two hours earlier in the day than nontornadic ones. The result is clear: a deeper boundary layer with steeper low-level lapse rates in the tornadic composite. Even so, the greater depth of moisture in the tornadic case must be noted. Composite hodographs (Fig. 23) look similar except for the strengthening southerlies in the nontornadic profile, representing the incipient low-level jet later in the evening. There is also evidence of the veer-back-veer profile that appeared in several nontornadic events and may inhibit tornado production (Mulholland et al. 2015), while the tornadic hodograph is somewhat more sickle-shaped, as is common in tornadic environments (Esterheld and Giuliano 2008).

Near-field tornadic and nontornadic composite skew-Ts are overlaid in Fig. 24. The most noticeable thermodynamic difference between these is at the surface, where there is evidence of shallow cooling in the nontornadic composite but not in the tornadic one. Since such a pronounced difference in near-surface stability is not seen in the far-field composites, it seems likely that the near-field cooling in the nontornadic composite is at least in part storm-induced. This result suggests not only that storms can observably modify their inflow, but also that such modification can influence storm behavior in a way that makes physical sense—near-surface stabilization inhibiting tornado production. In the near-field composite hodographs (Fig. 25), the tornadic hodograph is slightly larger and there may be a hint of the veer-back profile above 1 km in the nontornadic one, but the hodographs are similar overall.

4. Selected field observations

MPEX and Mini-MPEX collected several unique observations of near-storm environments that merit detailed descriptions, even though they are single cases and may not be generalizable to other events. Some exemplify the above findings regarding supercell-environment interactions; others relate directly to the existing literature on severe weather environments. These brief case studies are presented below in chronological order.

a. Abrupt change in near-inflow hodographs on 15 May 2013

On the first day of MPEX, mobile sounding crews sampled a tornadic supercell in north-central Texas. Fig. 26 shows the location at which a sounding was released at 0003 UTC 16 May, less than 10 km south-southeast of the low-level mesocyclone center as determined by inspecting KFWD WSR-88D radial velocity data at the lowest tilt. The signal was lost just above 1 km AGL as the sonde encountered the storm. From the surface to that level, however, the sonde found a very large clockwise-curved hodograph with strong vertical wind shear immediately above the ground (Fig. 27). The slow, roughly eastward motion of the storm (determined from KFWD data) produced 534 $m^2 s^{-2}$ 0-1-km SRH. At 0017 UTC, after loss of the first sonde, another was launched from the same location (Fig. 28), still south-southeast of the center of low-level rotation. This location was presumably still in the storm’s inflow because the surface temperature and wind did not change from the first sounding. However, immediately after launch, the sonde encountered low-level winds markedly different from those observed only minutes earlier (Fig. 29). Instead of a large looping hodograph with an easterly wind component up to 1 km, the easterly component vanished quickly and wind speeds remained around 5-8 m s^{-1}—less than half of the largest magnitudes seen in the 0003 UTC profile. As a result, 0-1-km SRH dropped to 101 m^2 s^{-2} in the 0017 UTC sounding.

Such extreme variability in SRH at such a short distance from the supercell updraft seems likely to be storm-induced. The first sounding appeared to sample enhanced low-level flow directed toward the updraft to its north-northwest. The second sounding's veered flow in the lowest kilometer has no obvious explanation, but could indicate the passage of a boundary layer roll slightly decoupled from the surface. The very small difference in storm-relative location between these wind profiles suggests that storms' modifications to the wind field may be more localized and have sharper gradients at their edges than suggested in the Parker (2014) composites, which portray a broad but modest increase in SRH across the near inflow. This would at least partially explain the difficulty of consistently observing this augmented low-level flow with a single radiosonde [or a single wind profiler, as in Brooks et al. (1994b)].

b. Subsidence and drying on 18 May 2013

On 18 May 2013, MPEX mobile sounding crews near Russell in central Kansas sampled the distant inflow of a tornadic supercell to the west, near Hays, Kansas. Another tornadic supercell approached from the southwest (near Rozel, Kansas), with its downstream anvil spreading toward the sounding crews, which were arranged roughly in a small equilateral triangle with sides of ~20 km. Soundings from 0001, 0005, and 0041 UTC (Figs. 30, 31, and 32) depict progressive subsidence and drying, eventually yielding a deep, dry, well-mixed layer more suggestive of a dryline passage than of a severe thunderstorm environment. While Barnes (1978) noted low-level subsidence ahead of a supercell updraft, this change was far more pronounced, and likely represents adiabatic warming and drying of downdrafts originating in the distant downstream anvil (the saturated layer from ~550 hPa upward in the initial sounding). Approximately neutral stability in the initial profile's deep elevated mixed layer offered little resistance to parcels subsiding dry adiabatically from the bottom of the anvil to the top of the boundary layer, and the relatively shallow moisture in the boundary layer quickly mixed out from the top down. Although this modification of the near-storm environment occurred below the anvil far downstream, not in that storm's inflow, ingestion of the resulting dry air was likely the main factor in the rapid decay of the supercell that moved east from near Hays, Kansas.

c. Environment of the 31 May 2013 El Reno tornado

MPEX observed the near-storm environment of the widest tornado on record, the EF3 El Reno, Oklahoma tornado of 31 May 2013, which reached a maximum diameter of 4.2 km (2.6 miles). A 2241 UTC CSU sounding (Figs. 33 and 34) and a 2300 UTC PU sounding (Figs. 35 and 36), respectively released 14 and 18 km south of the low-level mesocyclone, revealed similar environments before being ingested into the storm. Thermodynamically, the soundings were supportive of deep convection but not strikingly favorable for a historic tornado—appreciable CIN remained and LCL heights were only moderately low. The hodographs, however, were very large and contained extreme values of 0-1-km SRH relative to the observed eastward storm motion. While the background meso-β-scale environment near the intersection of a dryline and frontal boundary could feasibly approach the 2241 UTC profile's 0-1-km SRH of 475 $m^2 s^{-2}$, the 0-1-km SRH in excess of 700 $m^2 s^{-2}$ in the 2300 UTC profile was obviously enhanced by strong accelerations toward the nearby intense updraft. This was one motivation for pursuing near-field and far-field comparisons.

d. Sounding pairs preceding EF4 tornado on 9 May 2016

Several significant tornadoes occurred across south-central and southeastern Oklahoma on 9 May 2016. At initiation of the first tornadic supercell, a mesoscale boundary lingering from overnight and early-morning convection extended from near the dryline in central Oklahoma to near the Red River on the border of northeastern Texas and southeastern Oklahoma (Fig. 37). At 1952-1953 UTC, Mini-MPEX crews released soundings on the south side of the boundary, near Marietta, Oklahoma (Fig. 38), and on the north side, near Ardmore, Oklahoma (Fig. 39). The thermodynamic profiles were similar, with steep low-level lapse rates, negligible convective inhibition, and abundant moisture over a significant depth of the mixed boundary layer. Of particular interest are the hodographs, overlaid in Fig. 40. A relatively shallow layer of backed winds extending from near the surface to roughly 600 m AGL was present on the north side of the boundary and absent on the south side. Although the first tornadic supercell was merely a shower at the time of these soundings, the rightward motion observed 1-2 hours later after it matured was used to calculate 146 $m^2 s^{-2}$ 0-1-km SRH on the south side and 263 $m^2 s^{-2}$ on the north side. This is a remarkable difference for two soundings released 30 km apart across a subtle and somewhat diffuse boundary, and enhanced low-level hodographs on the north side almost certainly played a role in production of multiple significant tornadoes in southern Oklahoma in the hours after these soundings.

When the initial shower propagating northeastward from the dryline reached the boundary, it intensified rapidly into a tornadic supercell. At 2046 and 2052 UTC, soundings were launched in the near and far inflow (respectively) of the maturing supercell (Figs. 41 and 42). In the near inflow, 26 km southeast of the low-level mesocyclone center, steep low-level lapse rates persisted and there was no evidence of stabilization or convective inhibition resulting from cooling of the boundary layer. Hodographs are overlaid in Fig. 43. By this time, both mobile sounding crews had shifted northward toward the ongoing storm and were north of the aforementioned boundary. As a result, the hodographs were similar in size and shape. Though either would support a tornadic supercell, near-field enlargement of the low-level hodograph as seen in the composite hodographs was not observed in this case. It is possible that the young storm (only a shower some 50 minutes prior) had modified its environment less than a long-lived, mature supercell (e.g., 31 May 2013). It is also possible, in this case and in other cases, that non-storm-related variability of SRH in the mesoscale environment (Markowski et al. 1998b) was indistinguishable from any storm-induced enhancement that may have been present. The lack of any near-field enlargement of the hodograph suggests that future studies should attempt to examine the dependence of storm-induced changes to the environment on time from storm or mesocyclone initiation. Sample sizes in this study are too small to generalize anything about such time dependence.

e. 9 May 2016 rear-flank tornado

As the Katie-Sulphur supercell was weakening and new storms were maturing in its inflow to the southeast, another sounding (Figs. 44 and 45) was launched behind these new cells at 2204 UTC. The release location is plotted with radar reflectivity in Fig. 46. The southern part of the supercell cluster had produced rainfall at the launch location; the crew observed wet surfaces all around. The new storms had not yet generated a coherent cold pool, and full insolation immediately behind them maintained a thermodynamically favorable environment for severe weather directly along the rear of the cluster with extremely steep low-level lapse rates—in excess of 10 K km^{-1} over the lowest 1 km, owing to strong surface heat flux. (Marked superadiabatic layers near the surface were commonly observed in Mini-MPEX and are believed to be physical, as sounding crews took care to minimize exposure errors.) This unusual scenario likely contributed to production of a weak tornado in rural Johnston County, Oklahoma, that lasted for about seven minutes (Fig. 47). As viewed from the KTLX WSR-88D in Oklahoma City, this tornado was associated with only a very faint tendril of reflectivity extending from the rear of the cluster (noted in Fig. 46) and had no clear velocity signature at any tilt. The tornado cannot be attributed to any deep or persistent mesocyclone. The surrounding cloud base viewed by the sounding crews appeared disorganized. However, the highly sheared environment was atypical of non-supercell tornadoes (e.g., Baumgardt and Cook 2006). It seems that this was a unique type of non-mesocyclone tornado made possible in part by the presence of steep low-level lapse rates at the rear of the supercell cluster, which facilitated both very rapid stretching of any ambient low-level vorticity and downward transport of angular momentum to help maintain the stronger low-level vertical wind shear (e.g., Parker 2012).

f. Short-lived low-precipitation storms of May 2016

On 23 May 2016, Mini-MPEX sampled a splitting low-precipitation (LP; Bluestein and Parks 1983) supercell in the eastern Texas Panhandle. The ambient environment appeared highly favorable for supercells, with ample deep shear, over 4000 J kg^{-1} MLCAPE, and negligible inhibition. However, midlevel relative humidity was extremely low. The storm's updraft was visibly narrow with a high cloud base, and the storm dissipated rapidly. Other storms in the immediate area followed a nearly identical evolution, but storms farther to the northeast (near Woodward, Oklahoma) and south (near Turkey, Texas) produced tornadoes late in the evening. Figs. 48 and 49 show a skew-T and hodograph characteristic of the eastern Texas Panhandle environment where storms dissipated.

A remarkably similar evolution of multiple weak LP supercells was sampled two days later on 25 May in south-central Kansas. Again, abundant CAPE (over 5000 J kg^{-1} MLCAPE in one sounding), negligible CIN, sufficient deep-layer shear, and a very dry mid-troposphere characterized the mesoscale environment. And again, deep convection that survived after sunset organized into a tornadic supercell at that time. Figs. 50 and 51 show a sounding characteristic of the south-central Kansas environment where storms dissipated.

These cases have four common characteristics. First, the short-lived storms moved away from the initiating boundary. In both LP cases, storms initiated near the east side of a somewhat diffuse dryline and propagated away from it before dissipating. The day between these two IOPs, 24 May, was a localized but intense tornado outbreak centered near Dodge City, Kansas. Supercells remaining on and near mesoscale boundaries in Kansas produced most or all of the tornadoes. Bluestein and Parks (1983) found no evidence of preexisting outflow boundaries influencing their small sample of LP storms. Second, low-level shear was weak. In both cases, winds below 3 km were about 10 m s^{-1} or weaker. Some hodographs had sections of clockwise curvature in low levels, but were small in magnitude; observed SRH in the 0-1-km layer ranged from 35 to 138 m^2 s^{-2} on 23 and 25 May. Third, midlevels were relatively dry. Grant and van den Heever (2014) demonstrated that simulated supercells become LP with intensifying midtropospheric dryness. Visually, the 23 and 25 May storms' updrafts did not appear to become undercut by outflow [the outcome simulated by Gilmore and Wicker (1998) in such an environment].

Instead, the updrafts simply evaporated. Fig. 52 is a photograph of a typical updraft on the evening of 25 May; the 23 May cells of interest were visually similar. This appearance is more consistent with James and Markowski's (2010) finding that entrainment of dry environmental air, not outflow-dominance, may be to blame for the weakening of updrafts amid dry midlevels. Fourth, subsidence inversions at varying midlevel altitudes were present in inflow soundings on both days. While synoptic-scale vertical velocities are negligible compared to those of deep convective updrafts, further drying of the ambient environment via subsidence might be meaningful. However, the storms themselves cannot be ruled out as causes of the observed subsidence inversions (e.g., Barnes 1978, Trapp et al. 2016) in near-field soundings. With these features in mind, a proposed conceptual model of these LP storms' evolution follows:

(1) A mesoscale boundary provides focused ascent, repeatedly producing towering cumulus that with time create a substantial, somewhat moistened entrainment zone. The absence of CIN allows the enhanced ascent at the boundary to go almost exclusively toward overcoming the remaining midlevel dry air, and a storm eventually initiates near the boundary.

(2) Ambient vertical shear contributes to vertical vorticity via tilting, resulting in modest midlevel rotation and basic supercell structure. However, low-level mesocyclogenesis—with its attendant hydrodynamic effects (e.g., Markowski

and Richardson 2010) that serve to strengthen the updraft and stretch vorticity—is retarded by a small low-level hodograph.

(3) Storm-relative midlevel flow is strong enough to prevent precipitation from wrapping around the upshear side of the rotating updraft, further delaying low-level mesocyclogenesis (Brooks et al. 1994a) and ensuring there is no precipitation barrier between the updraft and dry midlevel air on the back side, where Fankhauser (1971) observed entrainment of chaff into the updraft.

(4) Midlevel dryness induces LP structure, including an abnormally narrow and tilted updraft, and produces small deviant rightward motion (Grant and van den Heever 2014). This lack of storm motion to the right of the mean flow diminishes already meager SRH, further inhibiting mesocyclone development.

(5) The storm propagates out of the zone of ascent/low-level convergence associated with the initiating boundary.

(6) The updraft's narrow, tilted geometry owing to (5) and its nonhelicity (Lilly 1986b) owing to (3-5) cause it to entrain dry air at an ultimately fatal rate, as in James and Markowski (2010). Turbulent mixing and evaporative cooling dissipate the storm.

In short, in the presence of dry midlevels, a nascent updraft that fails to become sufficiently helical before losing the support of the initiating boundary will not mature. This at least partially explains the colloquial tendency of LP storms to be laminar-looking, spectacularly structured “barber poles”—only highly helical LPs can survive to maturity. (Future work might attempt to quantify “dry midlevels” and “sufficiently helical” for more quantitative interpretations of this result.)

The evolution of other storms in the 23-25 May sequence supports this model. On 23 May, supercells ongoing at sunset intensified after sunset and produced tornadoes northeast and south of where Mini-MPEX’s storms had dissipated. The onset of the low-level jet augmented low-level hodographs, enabling low-level mesocyclogenesis and making updrafts helical enough to persist. On 24 May, tornadic supercells near Dodge City, Kansas remained on or near mesoscale boundaries that enhanced ascent via low-level convergence, moistened the lower troposphere/entrainment zone, and provided ample low-level vorticity for rapid, intense mesocyclogenesis. As those cells were producing tornadoes, updrafts leaving the dryline just to the south-southwest in a superficially favorable environment did not attain comparable intensity. On 25 May, a supercell farther north in east-central Kansas produced a long-lived EF4 tornado by tracking directly along a subtle outflow boundary. Later that night, near and after sunset, a cluster of storms in northern Oklahoma abruptly grew into a significantly tornadic supercell as SRH increased with the onset of the low-level jet (see following section).

g. Significant nocturnal tornado on 25 May 2016

Figs. 53 and 54 depict a Mini-MPEX sounding launched 37 km east-southeast of a supercell that produced an EF2 tornado after nightfall near Carrier, Oklahoma. The sounding was released at 0256 UTC 26 May, while the tornado was in progress. The contrasts with the south-central Kansas environment sampled earlier in the day are clear: nocturnal cooling resulted in substantial CIN, the low-level jet increased low-level shear, and moistening occurred above the boundary layer. It should be noted that several showers and weak thunderstorms moved through this area prior to the formation of the tornadic supercell, and the sounding was released fairly near the forward flank precipitation. One or both of these, rather than a change in the background mesoscale environment, could explain the moister midlevels. This in fact appears to be the case, because a simultaneous distant inflow sounding to the southeast (Fig. 9) encountered the same extremely dry midlevels observed near earlier storms that failed to become supercellular.

Such close rawinsonde observations of significant nocturnal tornadoes are uncommon. Mead and Thompson's (2012) study using RAP analysis soundings found that in many cases of significant tornadoes after dark, a surge of low-level moisture overwhelms radiative cooling so that the low-level thermodynamic profile becomes more favorable for tornadoes, often actually increasing CAPE in spite of the diurnal cycle. This was not true of the Carrier tornado. Instead, low-level moisture remained roughly constant and the boundary layer stabilized, introducing considerable CIN. In keeping with the proposed model in the previous section, the low-level jet's enlargement of SRH (roughly doubled from earlier observations in south-central Kansas) resulted in a more helical midlevel updraft and far less entrainment of dry midlevel air than in earlier, diurnal attempts at storm organization. This apparently allowed the supercell to mature and produce a tornado despite the cooling boundary layer and increasing CIN. Finally, having emphasized the presence of steep low-level lapse rates in the near inflow of tornadic supercells earlier in this work, it is important to note their absence here. As in all other studies of supercell and tornado environments, there is no "silver bullet" for distinguishing tornadic environments from nontornadic ones.

5. Summary and conclusions

In this project, observed soundings from VORTEX2, MPEX, and Mini-MPEX were used to analyze interactions between supercells and their environments. To isolate storm-induced changes to the inflow environment, near-storm inflow soundings were compared to simultaneously observed profiles farther afield. These pairs of soundings were classified by tornado production. Changes in the near inflow were investigated both as distributions of perturbations in individual soundings and as differences in composite soundings.

The most consistently observed change in the inflow environment from the far field to the near field was an increase in SRH with tornadic supercells. While in some cases the background environment may have larger SRH closer to where the storm develops, the short distance (~30 km) between typical near and far soundings suggests that without the presence of any mesoscale boundary (which was ensured in selection of the sounding pairs), significant differences in SRH are likely storm-induced. Acceleration of low-level flow toward the updraft by storm-induced pressure perturbations is the most intuitive mechanism for enlargement of near-field hodographs and SRH. There were several cases—notably, the 9 May 2016 significantly tornadic supercell near Katie, Oklahoma—in which this effect was not observed. Some observations suggest that substantial enhancement of the low-level wind field is confined to a relatively small sector of the inflow and may require a mature supercell, and preexisting mesoscale variability of SRH complicates near-field and far-field comparisons.

Steep, sometimes extreme, low-level lapse rates were often observed in the inflow of supercells, and in some cases may have contributed to tornadogenesis. Steep 0-1-km lapse rates tended to persist into the near inflow of tornadic supercells in spite of anvil shading; there was no consistent evidence of diabatic cooling or stabilization in the near inflow of tornadic storms. Anvil shading is well documented in existing literature. It seems likely that its effects are more pronounced directly along the storm's path, where parcels have a longer residence time under the anvil. However, rawinsonde observations suggest that this effect is often absent slightly right of the storm's path, even at very close range (~20 km). Updraft ingestion of several radiosondes from such locations during MPEX and Mini-MPEX implies that such parcels can be direct inflow parcels, so this is an important finding.

These two common characteristics of the near inflow of tornadic supercells may be related. In idealized numerical simulations, Parker (2012) explored the effect of lapse rates on the intensification of low-level vortices. In environments with dry adiabatic lapse rates (neutral stability) in the lower troposphere, convective heating cannot be dispersed by gravity waves, concentrating it in the updraft region. In the compensating subsidence around an updraft, neutral stability also enables downward displacement of parcels from aloft with higher angular momentum. In the simulations, these two effects enhanced low-level vortex intensification, resulting in increased near-surface pressure falls. Steep low-level lapse rates observed to persist even under the anvil could make tornadic supercells more efficient at enlarging 0-1-km AGL hodographs in the near inflow, as was observed in this study.

The first step of any future work in this area should be to collect a broader sample of simultaneous inflow sounding pairs, if possible; the current set of tornadic pairs is centered much earlier in the day than the nontornadic pairs, and the entire dataset consists only of springtime Great Plains environments with moderate to extreme instability. A larger number of soundings might also allow interpolation to a three-dimensional grid and creation of truly vertical near-field profiles, as opposed to observed soundings that drift with the flow. Denser spatiotemporal sampling of individual storms is also desirable for describing the spatial extent of storm-induced changes and their dependence on the time elapsed since storm initiation. This would require use of additional mobile sounding vehicles, unmanned aerial systems, or both. Denser sampling might also clarify the spatial variation of the effects of anvil shading. Further research might attempt to connect near-inflow low-level lapse rates to low-level flow enhancement more definitively, with both observations and numerical modeling.

Operational implications of the near-far inflow comparisons are currently limited; the findings provide context for interpreting observations in the near inflow of supercells, but such data are seldom available to forecasters in real time. Some of the individual case studies presented are likely of more immediate operational utility as examples of unusual, unexpected, or rarely sampled storm behavior. However, it is hoped that this research is a step from the existing knowledge of favorable environments toward understanding how environmental air parcels become directly involved in severe weather production within a storm.

References

American Meteorological Society, 2012: AMS glossary. Accessed 10 March 2016. [Available online at http://glossary.ametsoc.org/wiki/supercell.]

Barnes, S. L., 1970: Some aspects of a severe, right-moving thunderstorm deduced from mesonetwork rawinsonde observations. *J. Atmos. Sci.*, **27**, 634–648, doi: 10.1175/1520-0469(1970)027<0634:SAOASR>2.0.CO;2.

—, 1978: Oklahoma thunderstorms on 29-30 April 1970. Part I: Morphology of a tornadic storm. *Mon. Wea. Rev.*, **106**, 673–684, doi: 10.1175/1520-0493(1978)106<0673:OTOAPI>2.0.CO;2.

Battan, L. J., 1959: *Radar Meteorology*. University of Chicago Press, 161 pp.

Baumgardt, D. A., and K. Cook, 2006: Preliminary examination of a parameter to forecast environments conducive to non-mesocyclone tornadogenesis. *23rd Conf. Severe Local Storms*, St. Louis, MO, Amer. Meteor. Soc, 12.1.

Beebe, R. G., 1956: Tornado composite charts. *Mon. Wea. Rev.*, **84**, 127–142, doi: 10.1175/1520-0493(1956)084<0127:TCC>2.0.CO;2.

Bluestein, H. B., and C. R. Parks, 1983: A synoptic and photographic climatology of low-precipitation severe thunderstorms in the Southern Plains. *Mon. Wea. Rev.*, **111**, 2034–2046, doi: 10.1175/1520-0493(1983)111<2034:ASAPCO>2.0.CO;2.

Bolton, D., 1980: The computation of equivalent potential temperature. *Mon. Wea. Rev.*, **108**, 1046–1053, doi: 10.1175/1520-0493(1980)108<1046:TCOEPT>2.0.CO;2.

Brooks, H. E., C. A. Doswell III, and R. B. Wilhelmson, 1994a: The role of midtropospheric winds in the evolution and maintenance of low-level mesocyclones. *Mon. Wea. Rev.*, **122**, 126–136, doi: 10.1175/1520-0493(1994)122<0126:TROMWI>2.0.CO;2.

—, —, and J. Cooper, 1994b: On the environments of tornadic and nontornadic mesocyclones. *Wea. Forecasting*, **9,** 606–618, doi: 10.1175/1520-0434(1994)009<0606:OTEOTA>2.0.CO;2.

Browning, K. A., and F. H. Ludlam, 1962: Airflow in convective storms. *Quart. J. R. Meteor. Soc.*, **88**, 117–135.

—, and R. J. Donaldson, 1963: Airflow and structure of a tornadic storm. *J. Atmos. Sci.*, **20**, 535–545, doi: 10.1175/1520-0469(1963)020<0533:AASOAT>2.0.CO;2.

—, 1964: Airflow and precipitation trajectories within severe local storms which travel to the right of the winds. *J. Atmos. Sci.*, **21**, 634–639, doi: 10.1175/1520-0469(1964)021<0634:AAPTWS>2.0.CO;2.

Bunkers, M. J., B. A. Klimowski, J. W. Zeitler, R. L. Thompson, and M. L. Weisman, 2000: Predicting supercell motion using a new hodograph technique. *Wea. Forecasting*, **15**, 61–79, doi: 10.1175/1520-0434(2000)015<0061:PSMUAN>2.0.CO;2.

Craven, J. P., and H. E. Brooks, 2004: Baseline climatology of sounding derived parameters associated with deep, moist convection. *Natl. Wea. Dig.*, **28,** 13–24.

Davies, J., 2004: Estimations of CIN and LFC associated with tornadic and nontornadic supercells. *Wea. Forecasting*, **19**, 714–726, doi: 10.1175/1520-0434(2004)019<0714:EOCALA>2.0.CO;2.

Davies-Jones, R. P., 1984: Streamwise vorticity: The origin of updraft rotation. *J. Atmos. Sci.*, **41**, 2991–3006, doi: 10.1175/1520-0469(1984)041<2991:SVTOOU>2.0.CO;2.

Dessens, M., 1960: Severe hailstorms are associated with very strong winds between 6000 and 12000 m. *Geophys. Monograph*, **5**, 333–336.

Doswell III, C. A., and E. N. Rasmussen, 1994: The effect of neglecting the virtual temperature correction on CAPE calculations. *Wea. Forecasting*, **9,** 625–629, doi: 10.1175/1520-0434(1994)009<0625:TEONTV>2.0.CO;2.

Esterheld, J. M., and D. J. Giuliano, 2008: Discriminating between tornadic and non-tornadic supercells: A new hodograph technique. *Electron. J. Severe Storms Meteor.*, **3**, 1–50.

Fankhauser, J. C., 1971: Thunderstorm-environment interactions determined from aircraft and radar observations. *Mon. Wea. Rev.*, **99**, 171–192, doi: 10.1175/1520-0493(1971)099<0171:TIDFAA>2.3.CO;2.

Gilmore, M. S., and L. J. Wicker, 1998: The influence of midtropospheric dryness on supercell morphology and evolution. *Mon. Wea. Rev.*, **126**, 943–958, doi: 10.1175/1520-0493(1998)126<0943:TIOMDO>2.0.CO;2.

Grant, L. D., and S. C. van den Heever, 2014: Microphysical and dynamical characteristics of low-precipitation and classic supercells. *J. Atmos. Sci.*, **71**, 2604–2624, doi: 10.1175/JAS-D-13-0261.1.

Hart, J. A., and W. Korotky, 1991: The SHARP workstation v1.50 users guide. National Weather Service, NOAA, U.S. Department of Commerce, 30 pp. [Available from NWS Eastern Region Headquarters, 630 Johnson Ave., Bohemia, NY 11716.].

James, R. P., and P. M. Markowski, 2010: A numerical investigation of the effects of dry air aloft on deep convection. *Mon. Wea. Rev.*, **138**, 140–161, doi: 10.1175/2009MWR3018.1.

Klemp, J. B., and R. B. Wilhelmson, 1978: Simulations of right- and left-moving storms produced through storm splitting. *J. Atmos. Sci.*, **35**, 1097–1110, doi: 10.1175/1520-0469(1978)035<1097:SORALM>2.0.CO;2.

—, and R. Rotunno, 1983: A study of the tornadic region within a supercell thunderstorm. *J. Atmos. Sci.*, **40**, 359–377, doi: 10.1175/1520-0469(1983)040<0359:ASOTTR>2.0.CO;2.

Lemon, L. R., and C. A. Doswell III, 1979: Severe thunderstorm evolution and mesocyclone structure as related to tornadogenesis. *Mon. Wea. Rev.*, **107**, 1184– 1197, doi: 10.1175/1520-0493(1979)107<1184:STEAMS>2.0.CO;2.

Lilly, D. K., 1986a: The structure, energetics, and propagation of rotating convective storms. Part I: Energy exchange with the mean flow. *J. Atmos. Sci.*, **43**, 113–125, doi: 10.1175/1520-0469(1986)043<0113:TSEAPO>2.0.CO;2.

—, 1986b: The structure, energetics, and propagation of rotating convective storms. Part II: Helicity and storm stabilization. *J. Atmos. Sci.*, **43**, 126–140, doi: 10.1175/1520-0469(1986)043<0126:TSEAPO>2.0.CO;2.

Markowski, P. M., E. N. Rasmussen, J. M. Straka, and D. C. Dowell, 1998a: Observations of low-level baroclinity generated by anvil shadows. *Mon. Wea. Rev.*, **126**, 2942–2958, doi: 10.1175/1520-0493(1998)126<2942:OOLLBG>2.0.CO;2.

—, J. M. Straka, E. N. Rasmussen, and D. O. Blanchard, 1998b: Variability of storm-relative helicity during VORTEX. *Mon. Wea. Rev.*, **126**, 2959–2971, doi: 10.1175/1520-0493(1998)126<2959:VOSRHD>2.0.CO;2.

—, —, and —, 2002: Direct surface thermodynamic observations within the rear-flank downdrafts of nontornadic and tornadic supercells. *Mon. Wea. Rev.*, **130**, 1692–1721, doi: 10.1175/1520-0493(2002)130<1692:DSTOWT>2.0.CO;2.

—, C. Hannon, J. Frame, E. Lancaster, A. Pietrycha, R. Edwards, and R. L. Thompson, 2003: Characteristics of vertical wind profiles near supercells obtained from the Rapid Update Cycle. *Wea. Forecasting*, **18**, 1262–1272, doi: 10.1175/1520-0434(2003)018<1262:COVWPN>2.0.CO;2.

—, and Y. Richardson, 2010: *Mesoscale Meteorology in Midlatitudes*. Wiley, 430 pp.

Marwitz, J. D., 1972: The structure and motion of severe hailstorms. Part I: Supercell storms. *J. Appl. Meteor.*, **11**, 166–179, doi: 10.1175/1520-0450(1972)011<0166:TSAMOS>2.0.CO;2.

Mead, C. M., and R. L. Thompson, 2011: Environmental characteristics associated with nocturnal significant-tornado events in the central and southern Great Plains. *Electron. J. Severe Storms Meteor.*, **6** (6), 1–35.

Mulholland, J., J. W. Frame, and S. M. Steiger, 2015: A numerical investigation into the presence of veer-back-veer vertical wind profiles in supercell environments: A case study of 30 and 31 May 2013. *16th Conf. on Mesoscale Processes*, Boston, MA, Amer. Meteor. Soc., 3.7.

Nelson, S. P., 1976: Characteristics of multicell and supercell hailstorms in Oklahoma. *Proc. Second WMO Conf. on Weather Modification*, WMO-443, Boulder, 335–340.

Newton, C. W., and H. R. Newton, 1959: Dynamical interactions between large convective clouds and environment with vertical shear. *J. Meteor.*, **16**, 483–496, doi: 10.1175/1520-0469(1959)016<0483:DIBLCC>2.0.CO;2.

Nowotarski, C. J., and P. M. Markowski, 2016: Modifications to the near-storm environment induced by simulated supercell thunderstorms. *Mon. Wea. Rev.*, **144**, 273–293, doi: 10.1175/MWR-D-15-0247.1.

Parker, M. D., 2012: Impacts of lapse rates on low-level rotation in idealized storms. *J. Atmos. Sci.*, **69**, 538–559, doi: 10.1175/JAS-D-11-058.1.

—, 2014: Composite VORTEX2 supercell environments from near-storm soundings. *Mon. Wea. Rev.*, **142**, 508–529, doi: 10.1175/MWR-D-13-00167.1.

Potvin, C. K., K. L. Elmore, and S. J. Weiss, 2010: Assessing the impacts of proximity sounding criteria on the climatology of significant tornado environments. *Wea. Forecasting*, **25**, 921–930, doi: 10.1175/2010WAF2222368.1.

Rasmussen, E. N., and D. O. Blanchard, 1998: A baseline climatology of sounding-derived supercell and tornado forecast parameters. *Wea. Forecasting*, **13,** 1148–1164, doi: 10.1175/1520-0434(1998)013<1148:ABCOSD>2.0.CO;2.

—, 2003: Refined supercell and tornado forecast parameters. *Wea. Forecasting*, **18**, 530–535, doi: 10.1175/1520-0434(2003)18<530:RSATFP>2.0.CO;2.

Rotunno, R., 1981: On the evolution of thunderstorm rotation. *Mon. Wea. Rev.*, **109**, 577–586, doi: 10.1175/1520-0493(1981)109<0577:OTEOTR>2.0.CO;2.

—, and J. B. Klemp, 1982: The influence of the shear-induced pressure gradient on thunderstorm motion. *Mon. Wea. Rev.*, **110**, 136–151, doi: 10.1175/1520-0493(1982)110<0136:TIOTSI>2.0.CO;2.

—, and —, 1985: On the rotation and propagation of simulated supercell thunderstorms. *J. Atmos. Sci.*, **42**, 271–292, doi: 10.1175/1520-0469(1985)042<0271:OTRAPO>2.0.CO;2.

Smith, B. T., R. L. Thompson, J. S. Grams, C. Broyles, and H. E. Brooks, 2012: Convective modes for significant severe thunderstorms in the contiguous United States. Part I: Storm classification and climatology. *Wea. Forecasting*, **27**, 1114–1135, doi: 10.1175/WAF-D-11-00115.1.

Straka, J. M., E. N. Rasmussen, and S. E. Fredrickson, 1996: A mobile mesonet for finescale meteorological observations. *J. Atmos. Oceanic Technol.*, **13,** 921–936, doi: 10.1175/1520-0426(1996)013<0921:AMMFFM>2.0.CO;2.

Thompson, R. L., R. Edwards, and J. A. Hart, 2002: Evaluation and interpretation of the supercell composite and significant tornado parameters at the Storm Prediction Center. Preprints, *21st Conf. on Severe Local Storms,* San Antonio, TX, Amer. Meteor. Soc., J11–J14.

—, —, —, K. L. Elmore, and P. Markowski, 2003: Close proximity soundings within supercell environments obtained from the Rapid Update Cycle. *Wea. Forecasting*, **18**, 1243–1261, doi: 10.1175/1520-0434(2003)018<1243:CPSWSE>2.0.CO;2.

—, C. M. Mead, and R. Edwards, 2007: Effective storm-relative helicity and bulk shear in supercell thunderstorm environments. *Wea. Forecasting*, **22**, 102–115, doi: 10.1175/WAF969.1.

—, B. T. Smith, J. S. Grams, A. R. Dean, and C. Broyles, 2012: Convective modes for significant severe thunderstorms in the contiguous United States. Part II: Supercell and QLCS tornado environments. *Wea. Forecasting*, **27**, 1136–1154, doi: 10.1175/WAF-D-11-00116.1.

Trapp, R. J., and Coauthors, 2016: Mobile radiosonde deployments during the Mesoscale Predictability Experiment (MPEX): Rapid and adaptive sampling of upscale convective feedbacks. *Bull. Amer. Meteor. Soc.*, **97**, 329–336, doi: 10.1175/BAMS-D-14-00258.1.

Weisman, M. L., and Coauthors, 2015: The Mesoscale Predictability Experiment (MPEX). *Bull. Amer. Meteor. Soc.*, **96**, 2127–2149, doi: 10.1175/BAMS-D-13-00281.1.

Weygandt, S. S., and Coauthors, 2015: Rapid Refresh: version 2 upgrade at NCEP and work toward version 3 and the North American Rapid Refresh Ensemble (NARRE). *5th Conf. on Transition from Research to Operations*, Phoenix, AZ, Amer. Meteor. Soc., 4.1.

Whiting, R. M., and R. E. Bailey, 1957: Some meteorological relationships in the prediction of tornadoes. *Mon. Wea. Rev.*, **85**, 141–150, doi: 10.1175/1520-0493(1957)085<0141:SMRITP>2.0.CO;2.

Williams, R. J., 1976: Surface parameters associated with tornadoes. *Mon. Wea. Rev.*, **104**, 540–545, doi: 10.1175/1520-0493(1976)104<0540:SPAWT>2.0.CO;2.

Appendix: Figures

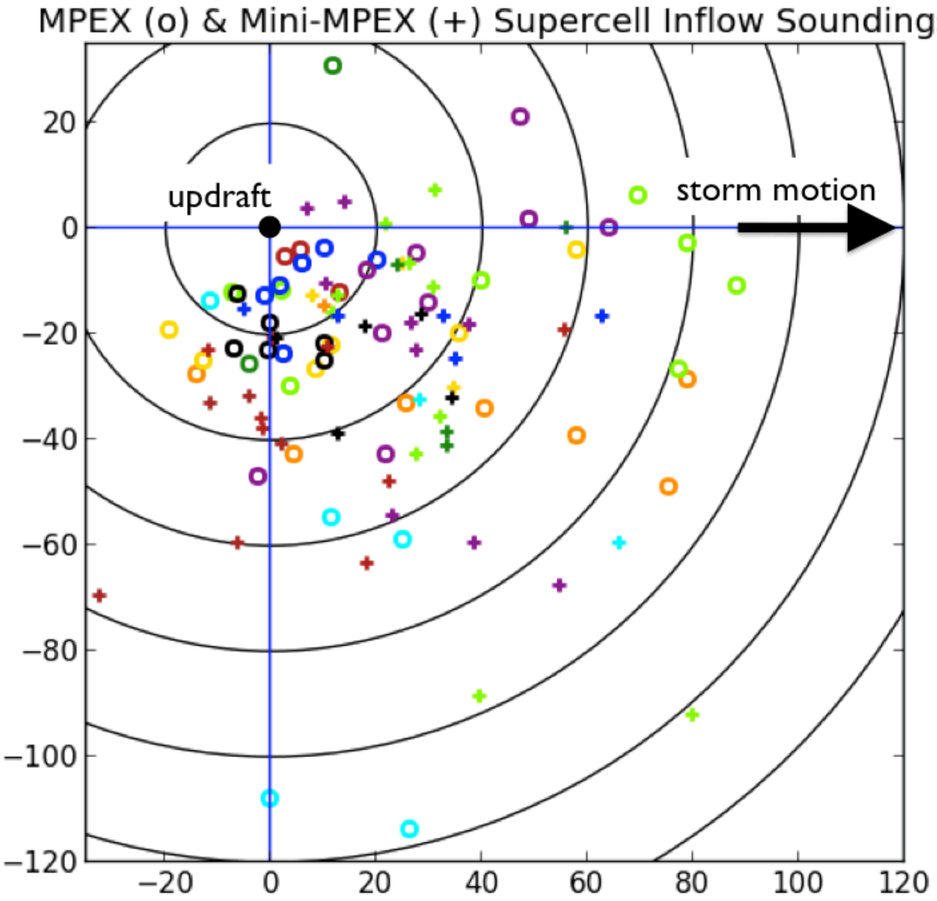

Fig. 1: Storm-relative release points of all supercell inflow soundings collected by MPEX and Mini-MPEX. Circles denote MPEX soundings; crosses denote Mini-MPEX soundings. Different colors denote different severe weather events within each project. The updraft is at the origin and observed storm motion over the subsequent hour is along the positive x-axis. Rings are intervals of 20 km.

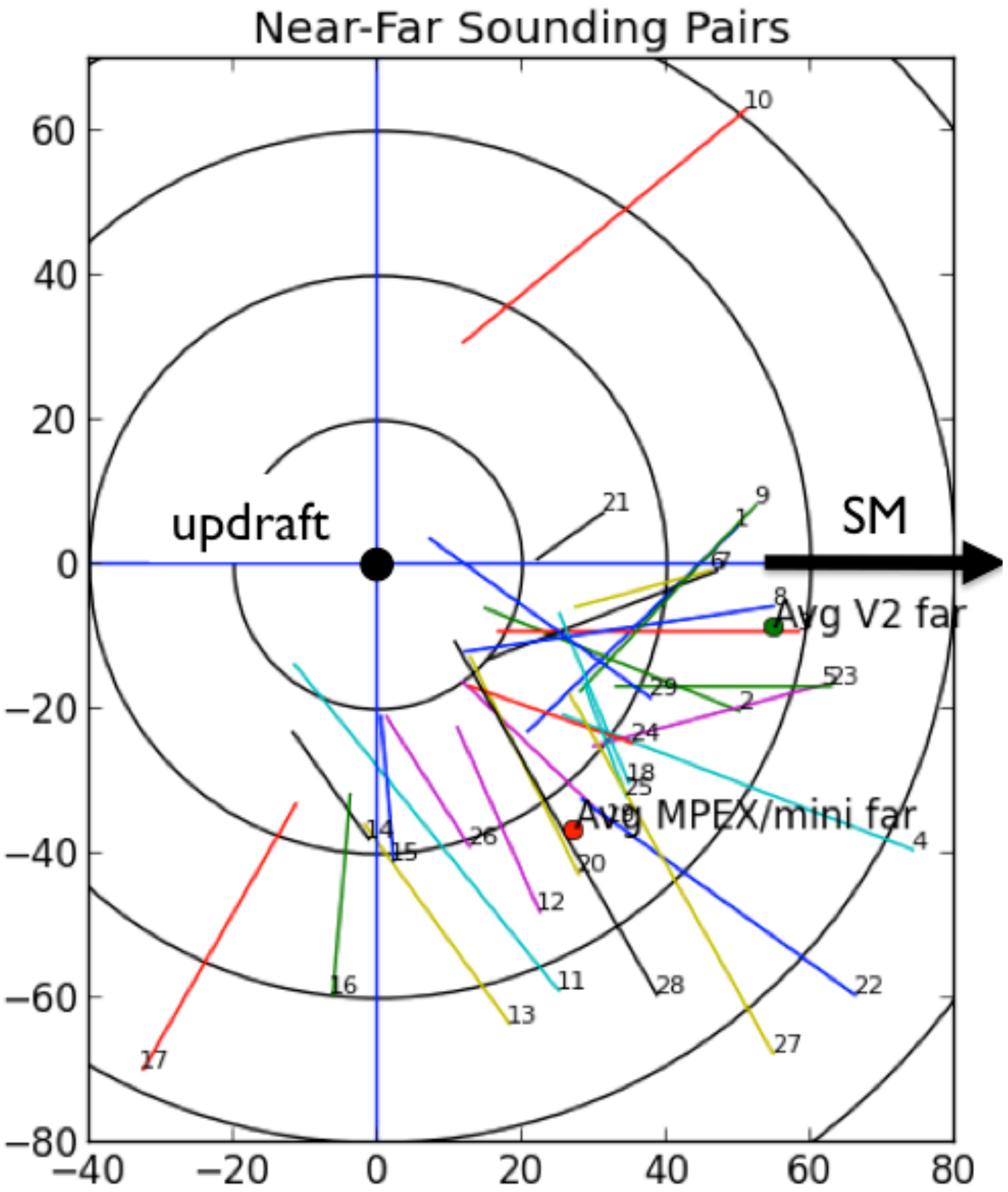

Fig. 2: Line segments connecting the storm-relative (as in Fig. 1) release points of approximately simultaneous near-far sounding pairs. Mean far-field locations for different projects are noted.

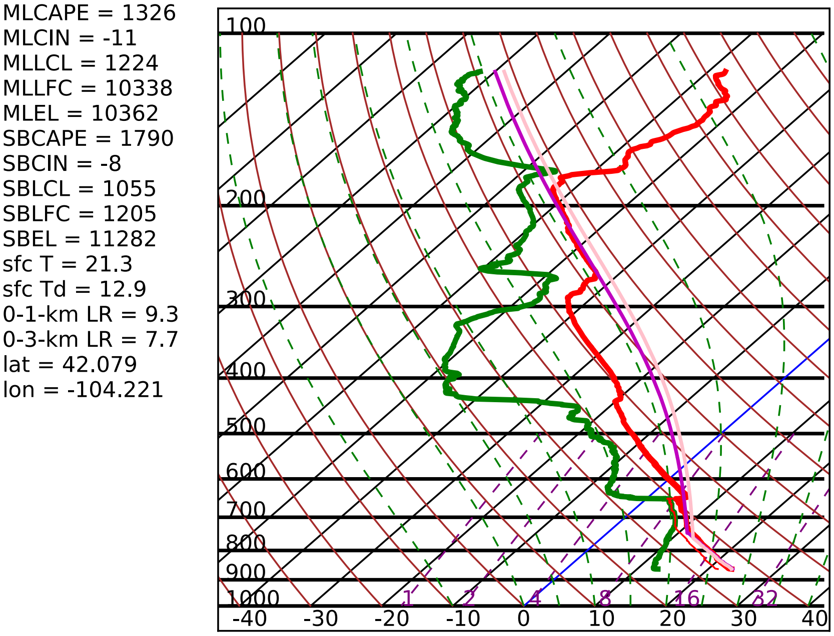

MLCAPE = 1326
MLCIN = -11
MLLCL = 1224
MLLFC = 10338
MLEL = 10362
SBCAPE = 1790
SBCIN = -8
SBLCL = 1055
SBLFC = 1205
SBEL = 11282
sfc T = 21.3
sfc Td = 12.9
0-1-km LR = 9.3
0-3-km LR = 7.7
lat = 42.079
lon = -104.221

Fig. 3: Skew-*T* log-*p* diagram of near inflow sounding from 0025 UTC 22 May 2010. Here and in subsequent soundings, the bold red line is virtual temperature while the thin red line is temperature. Where parcel traces are plotted, the magenta line represents a mixed-layer parcel and the pink line represents a surface-based parcel.

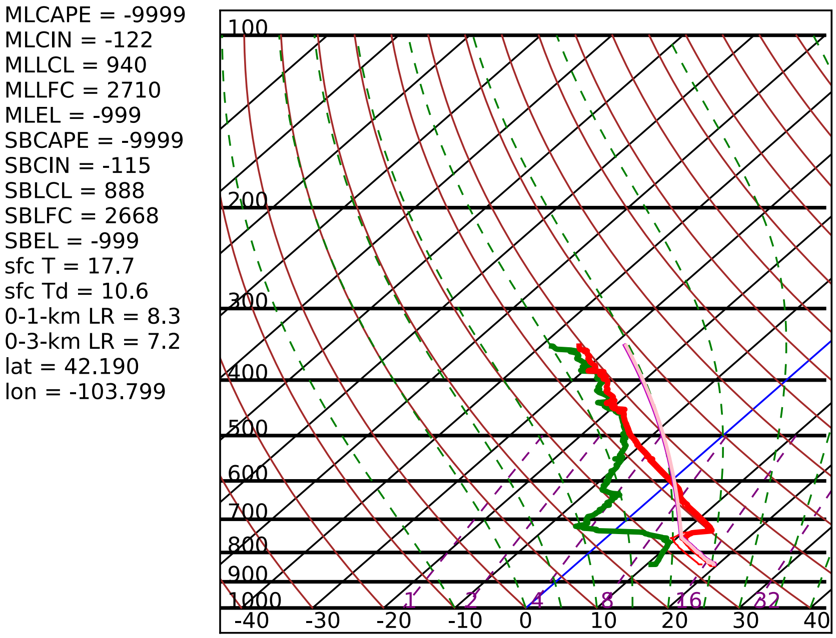

Fig. 4: Skew-*T* log-*p* diagram of far inflow sounding from 0013 UTC 22 May 2010.

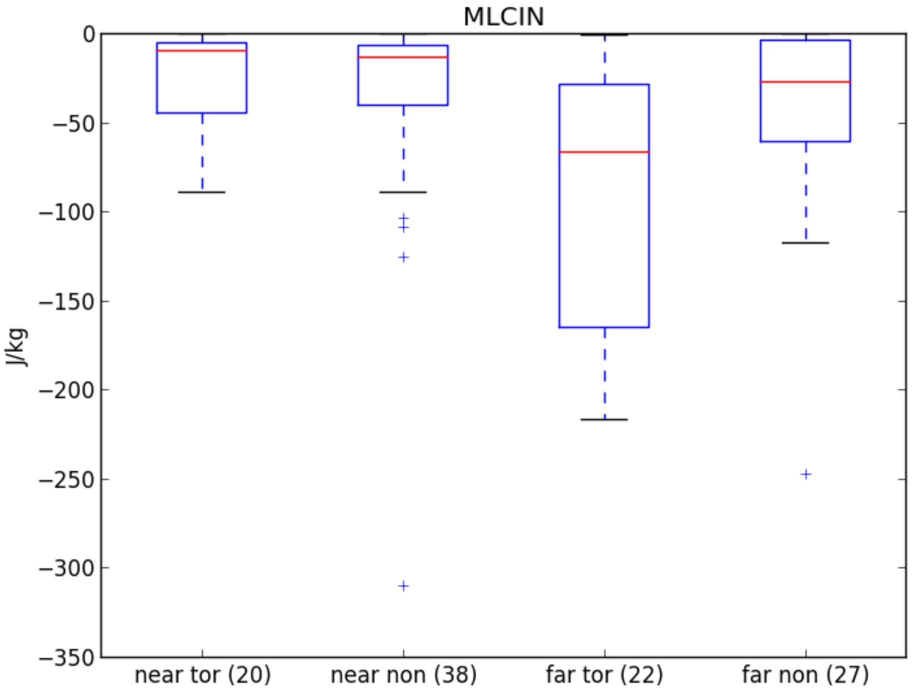

Fig. 5: Distributions of MLCIN for subsets of supercell inflow soundings. Here and in all following boxplots, whiskers extend to the most extreme values within 1.5 times the interquartile range of the nearest quartile, with more extreme values plotted as single points.

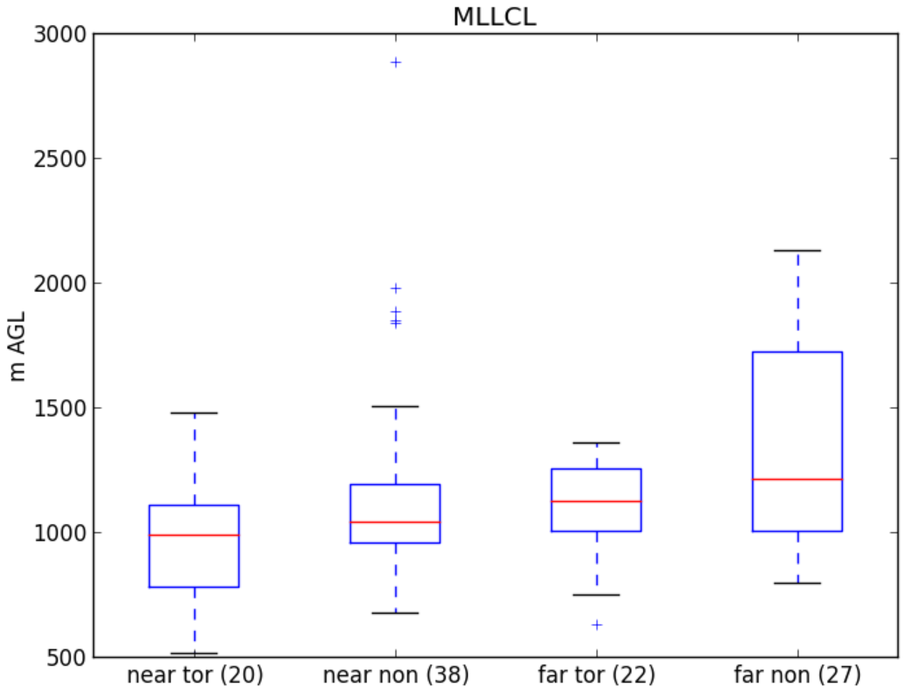

Fig. 6: Distributions of MLLCL height for subsets of supercell inflow soundings.

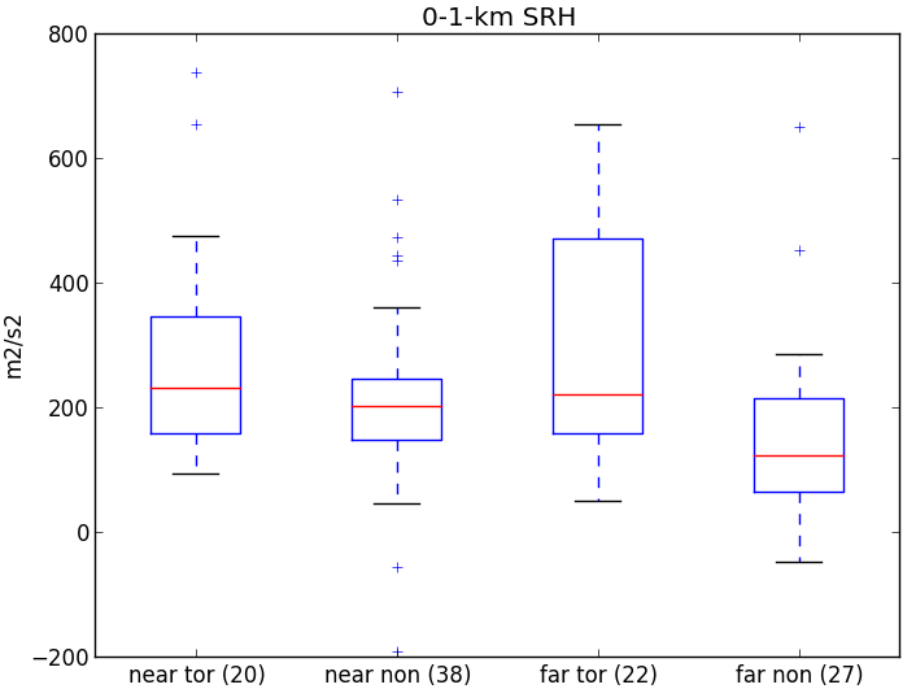

Fig. 7: Distributions of 0-1-km SRH for subsets of supercell inflow soundings.

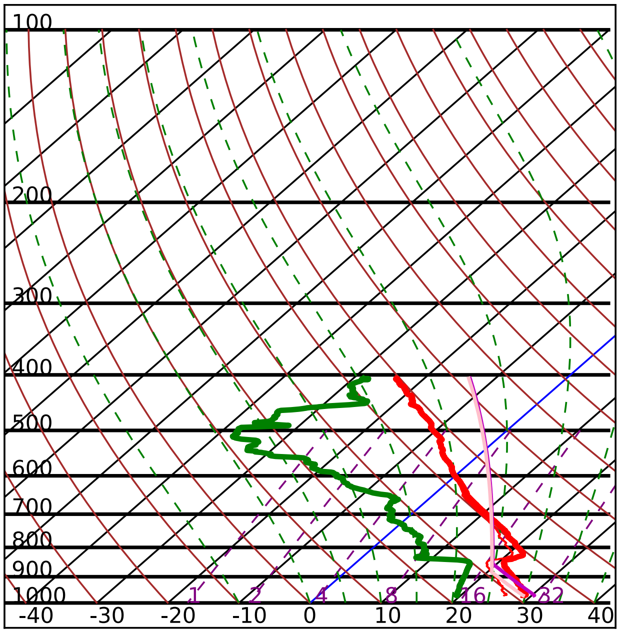
MLCAPE = -9999
MLCIN = -141
MLLCL = 1099
MLLFC = 2641
MLEL = -999
SBCAPE = -9999
SBCIN = -190
SBLCL = 826
SBLFC = 2674
SBEL = -999
sfc T = 26.1
sfc Td = 19.4
0-1-km LR = 7.0
0-3-km LR = 6.7
lat = 35.377
lon = -96.310

Fig. 8: Skew-*T* log-*p* diagram of inflow sounding released 41 km from a tornadic supercell at 0011 UTC 20 May 2013.

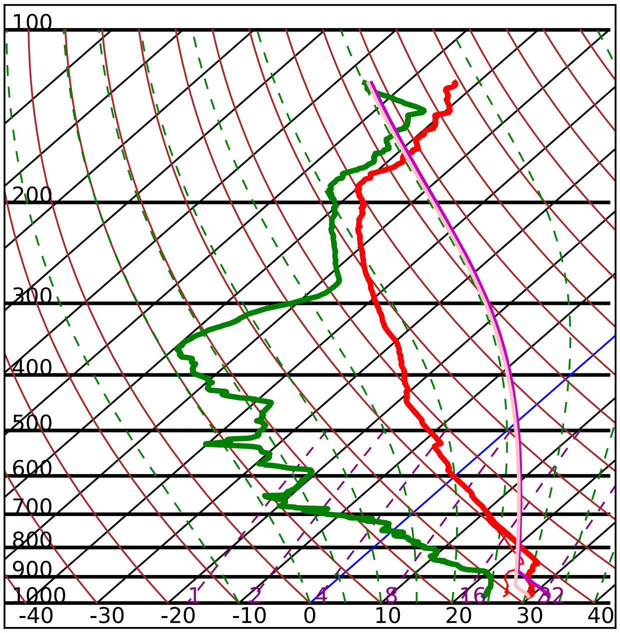
MLCAPE = 5182
MLCIN = -56
MLLCL = 834
MLLFC = 1766
MLEL = 13138
SBCAPE = 4991
SBCIN = -102
SBLCL = 357
SBLFC = 13108
SBEL = 13138
sfc T = 26.2
sfc Td = 23.4
0-1-km LR = 4.0
0-3-km LR = 6.7
lat = 36.414
lon = -97.328

Fig. 9: Skew-*T* log-*p* diagram of inflow sounding released 65 km from a tornadic supercell at 0256 UTC 26 May 2016.

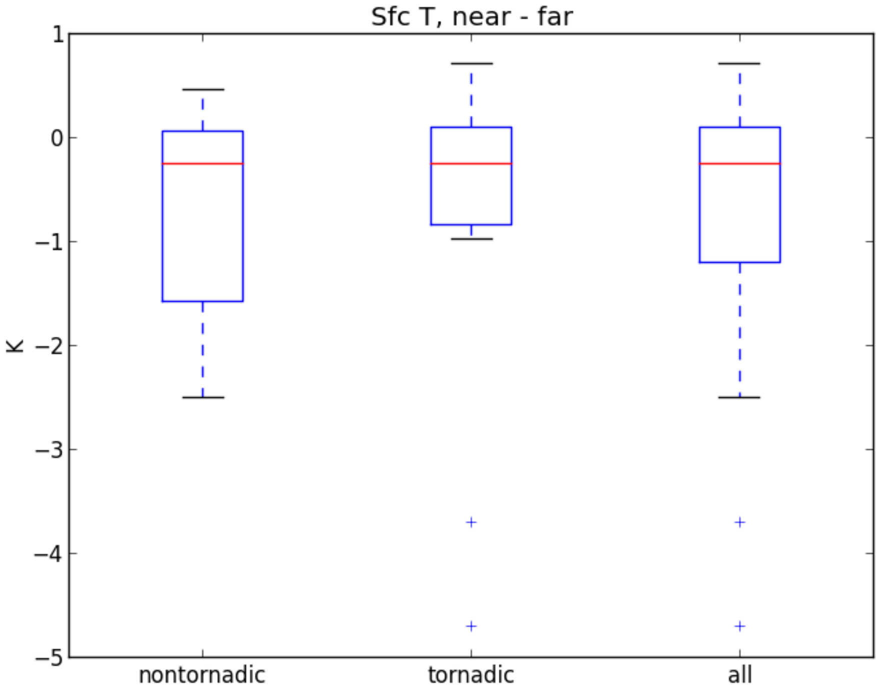

Fig. 10: Distributions of surface temperature perturbations for inflow sounding pairs. Here and in following plots of perturbation quantities, these perturbations are defined as the near-field value minus the far-field or background value.

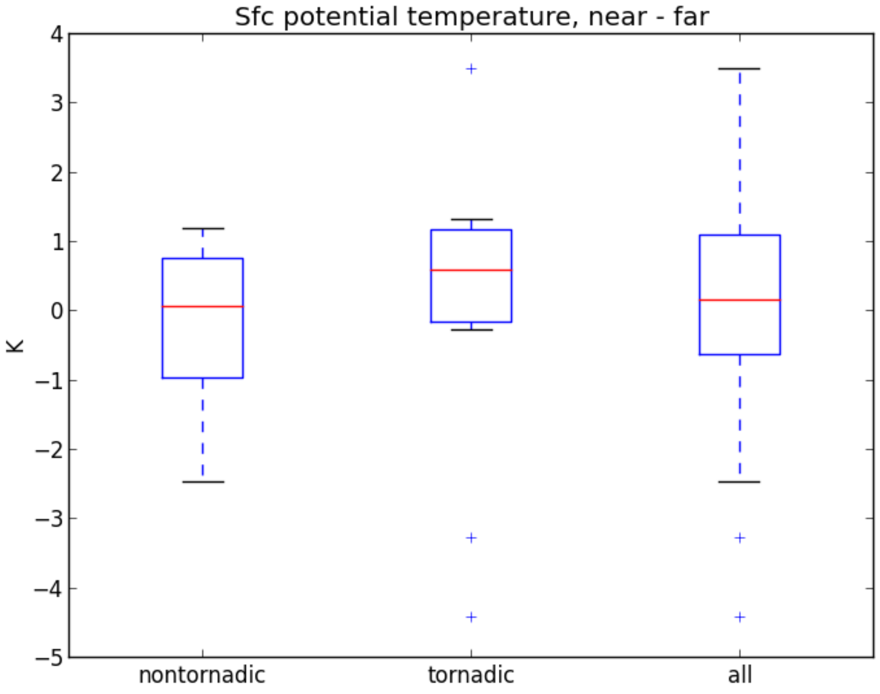

Fig. 11: Distributions of surface potential temperature perturbations for inflow sounding pairs.

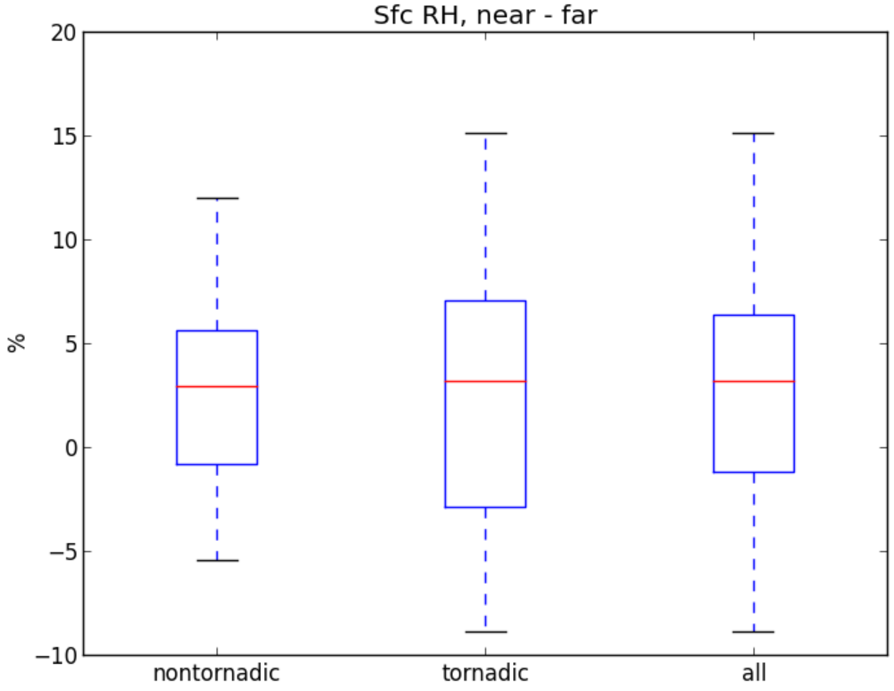

Fig. 12: Distributions of surface relative humidity perturbations for inflow sounding pairs.

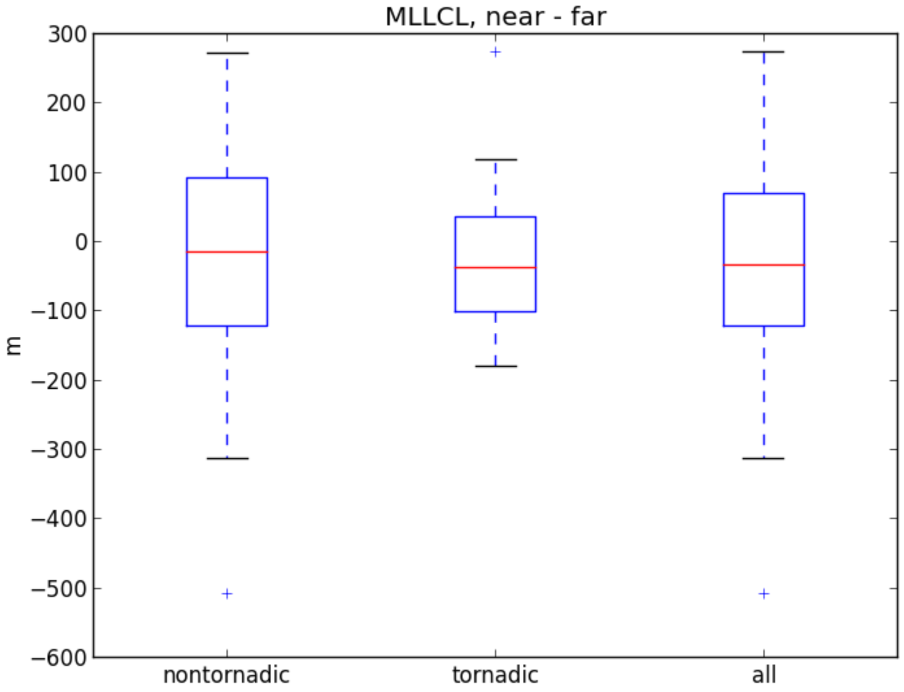

Fig. 13: Distributions of MLLCL perturbations for inflow sounding pairs.

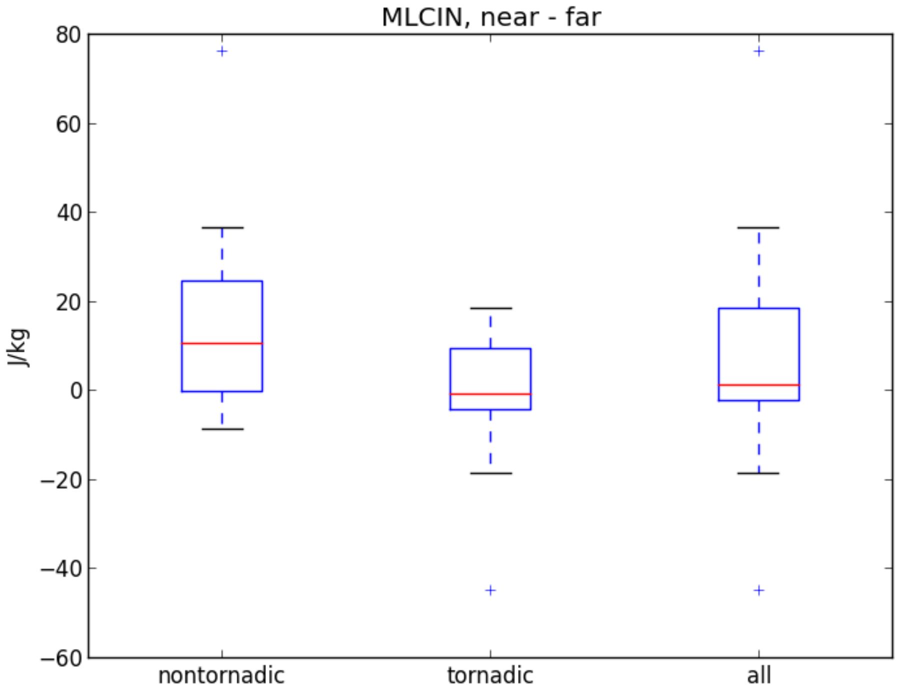

Fig. 14: Distributions of MLCIN perturbations for inflow sounding pairs.

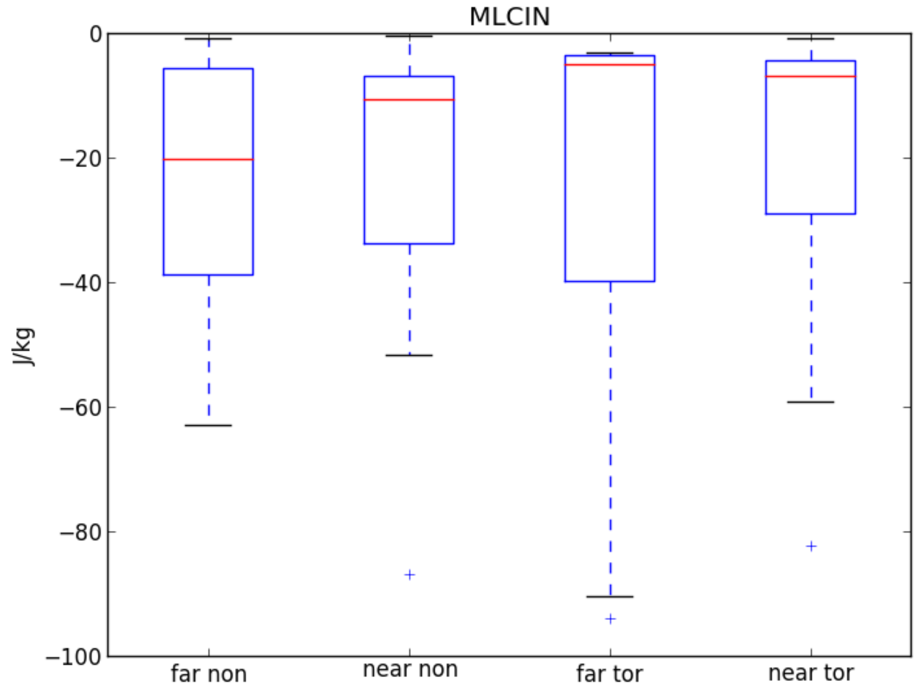

Fig. 15: Distributions of MLCIN for subsets of soundings used in compiling inflow sounding pairs.

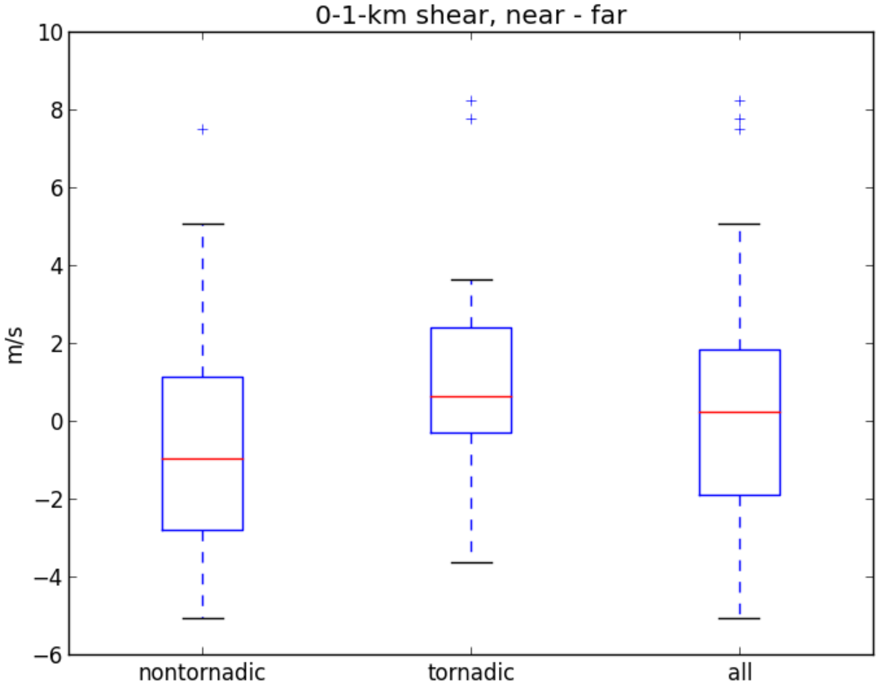

Fig. 16: Distributions of 0-1-km shear magnitude perturbations for inflow sounding pairs.

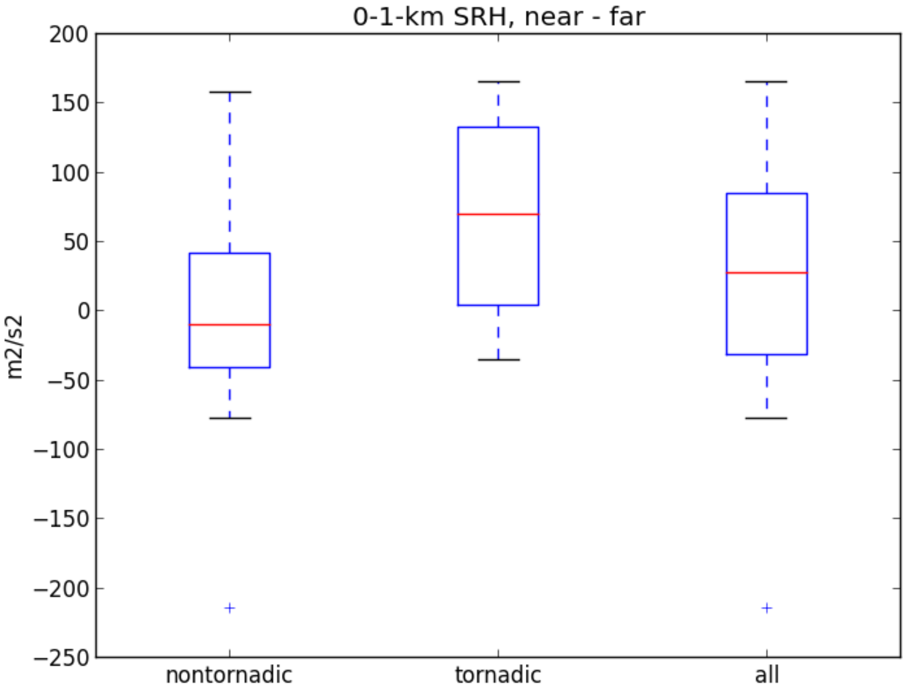

Fig. 17: Distributions of 0-1-km SRH perturbations for inflow sounding pairs.

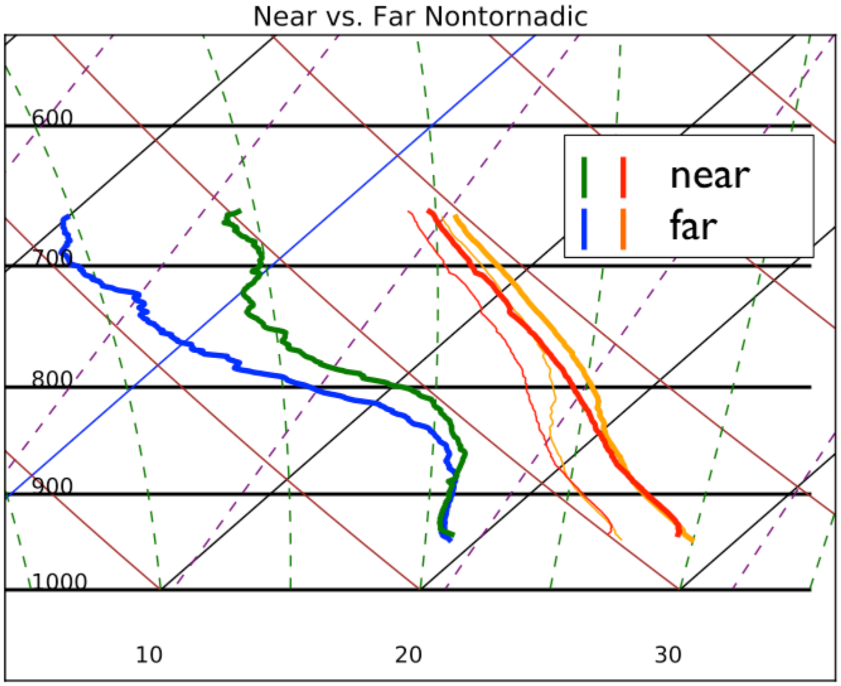

Fig. 18: Skew-*T* log-*p* diagram of near-field and far-field nontornadic composite soundings.

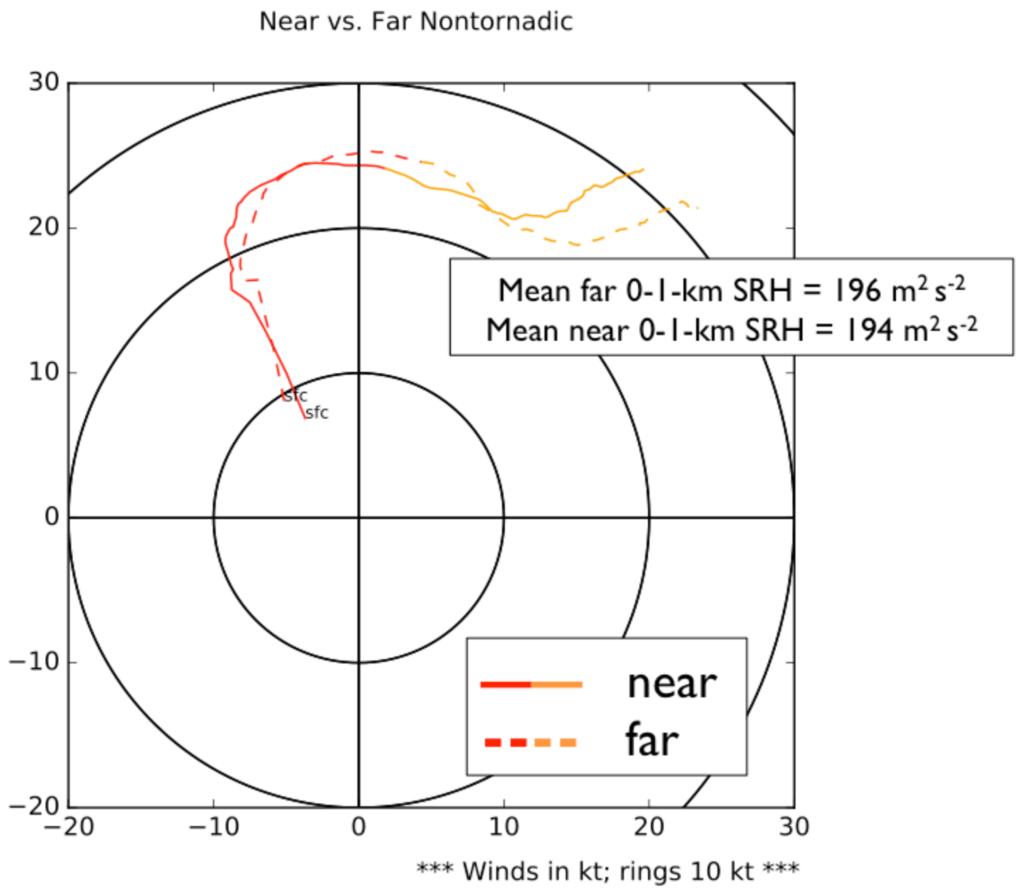

Fig. 19: Hodographs of near-field and far-field nontornadic composite soundings. Here and in other hodographs, rings are intervals of 10 km. Red sections extend from the surface to 1 km AGL; yellow-orange sections extend from 1 to 3 km AGL.

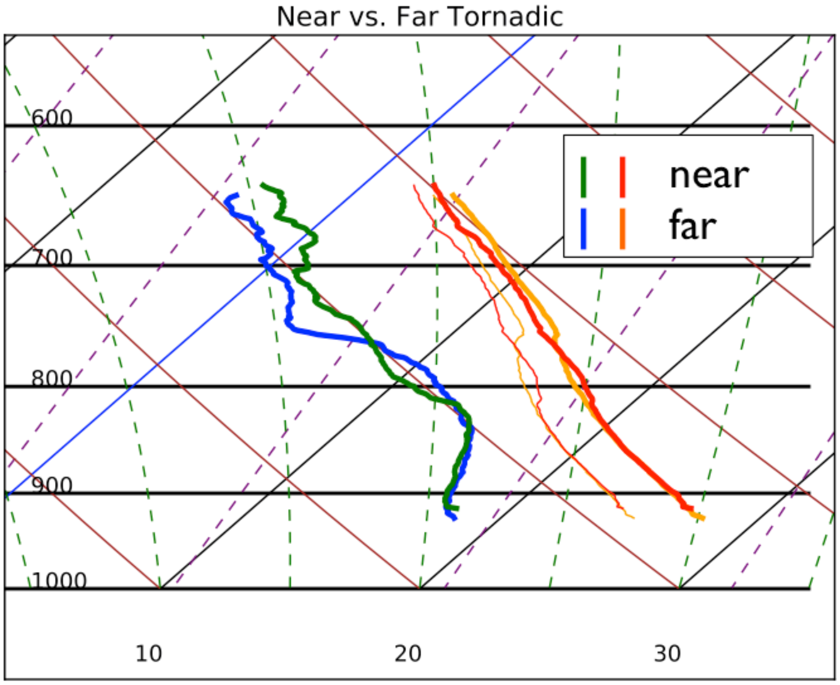

Fig. 20: Skew-*T* log-*p* diagram of near-field and far-field tornadic composite soundings.

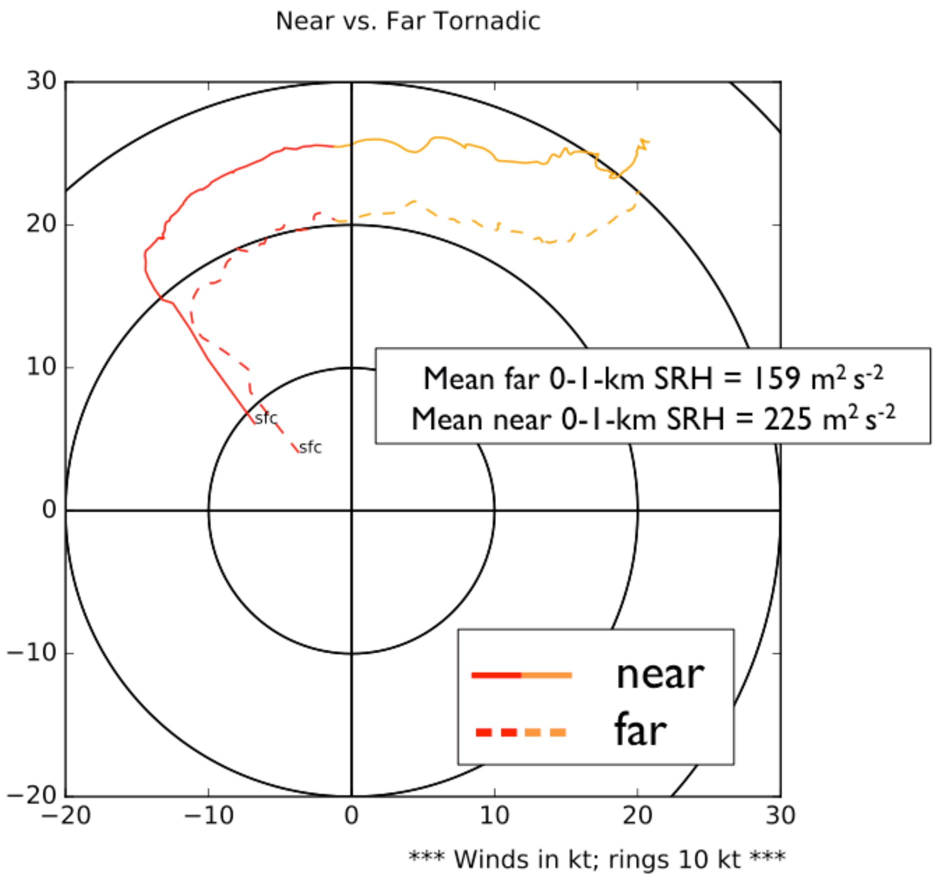

Fig. 21: Hodographs of near-field and far-field tornadic composite soundings.

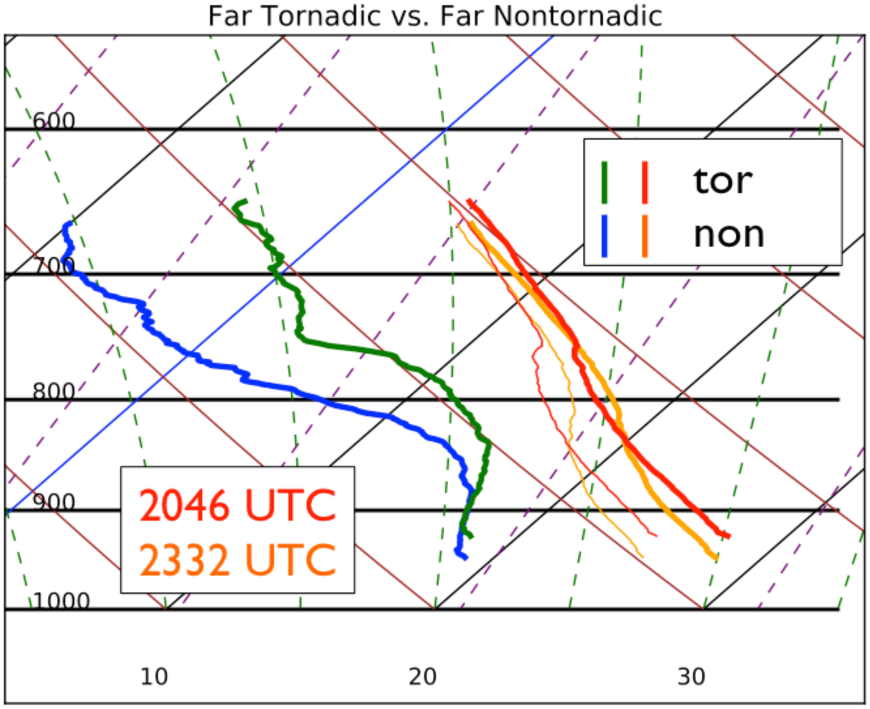

Fig. 22: Skew-*T* log-*p* diagram of tornadic and nontornadic far-field composite soundings. The large difference in mean time of day is noted.

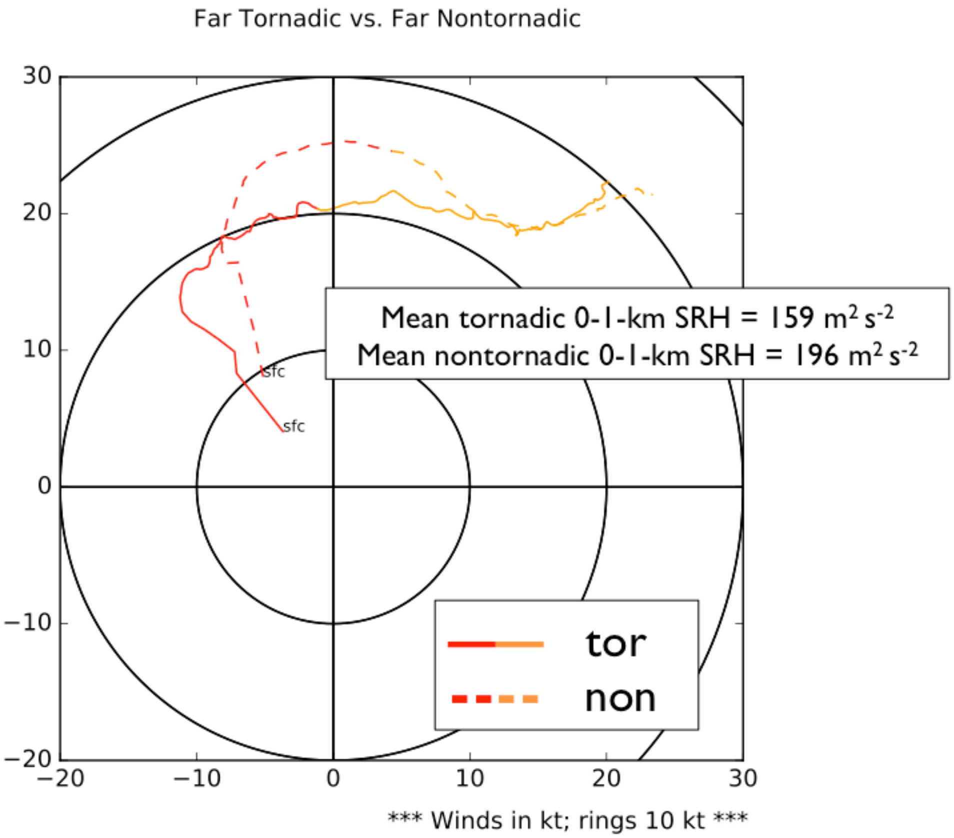

Fig. 23: Hodographs of tornadic and nontornadic far-field composite soundings.

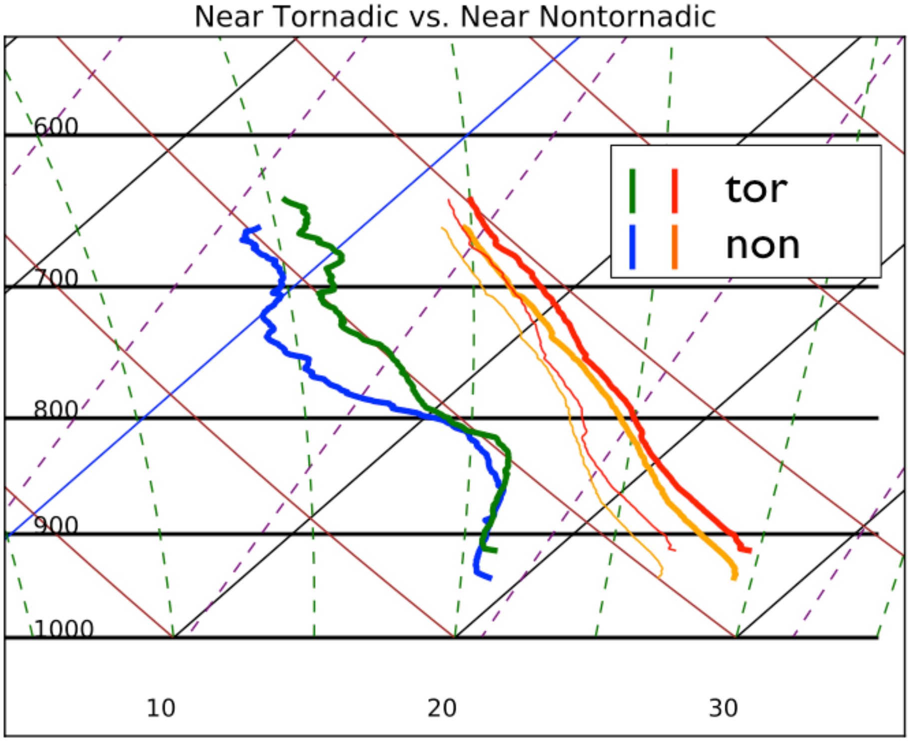

Fig. 24: Skew-*T* log-*p* diagram of tornadic and nontornadic near-field composite soundings.

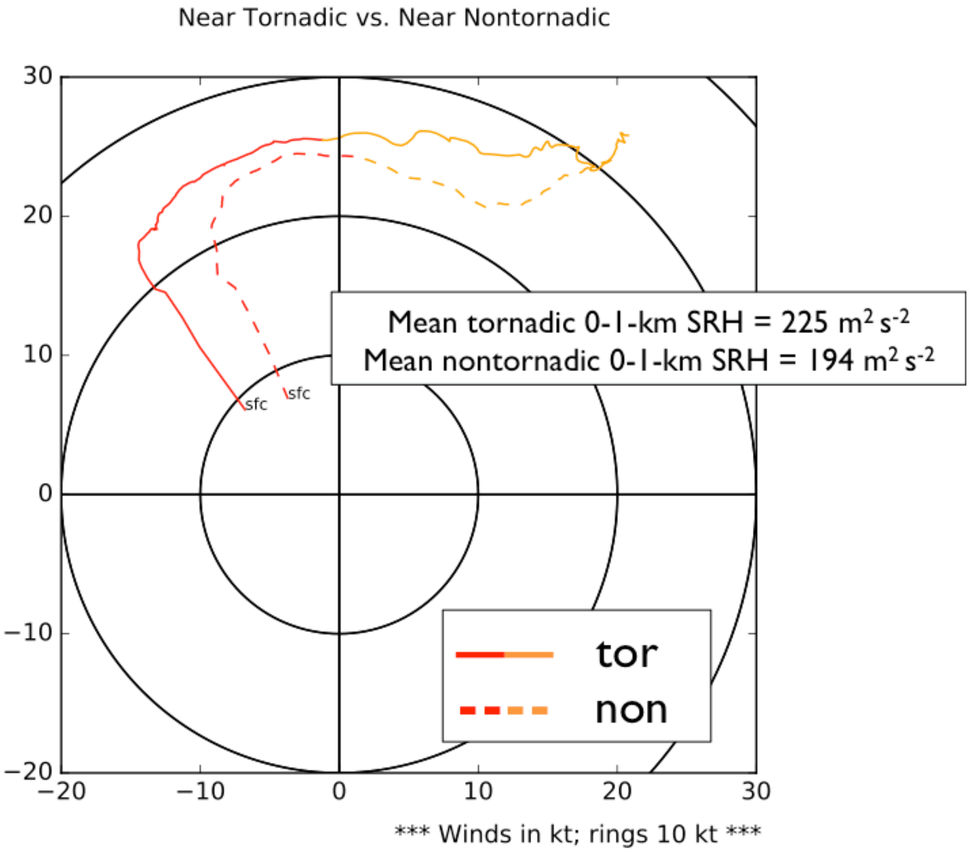

Fig. 25: Hodographs of tornadic and nontornadic near-field composite soundings.

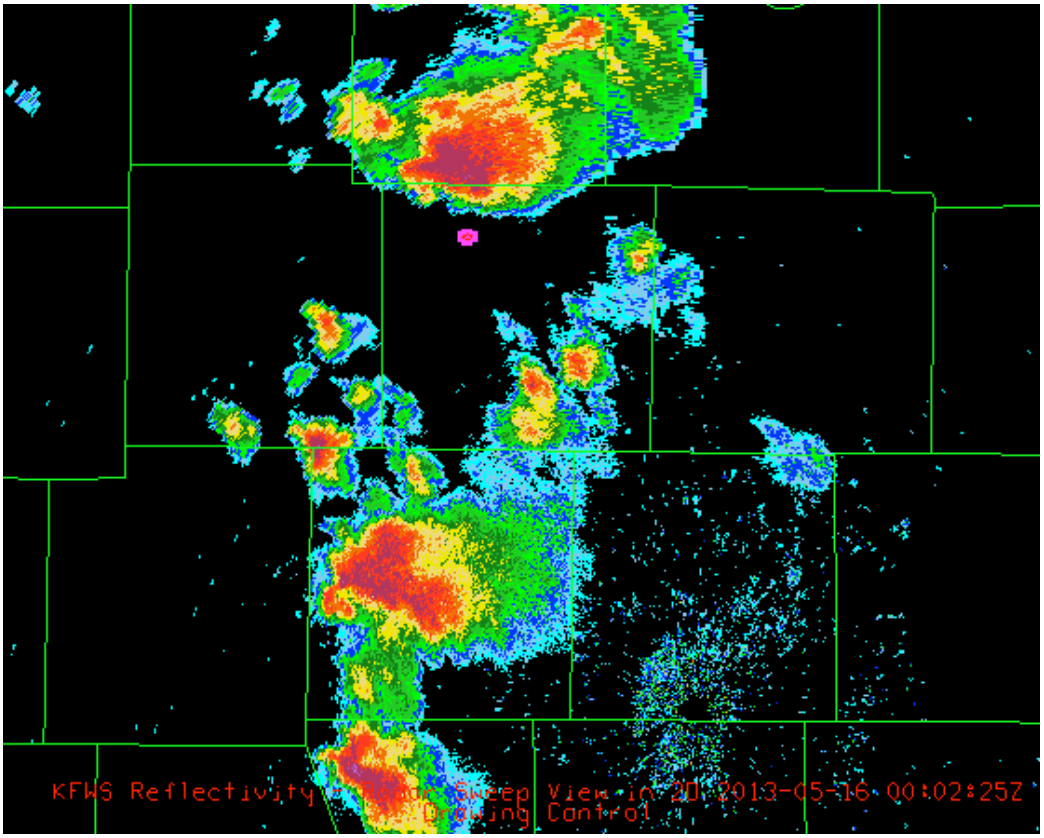

Fig. 26: Release point of 0003 UTC 16 May 2013 MPEX sounding, overlaid with KFWD WSR-88D radar reflectivity.

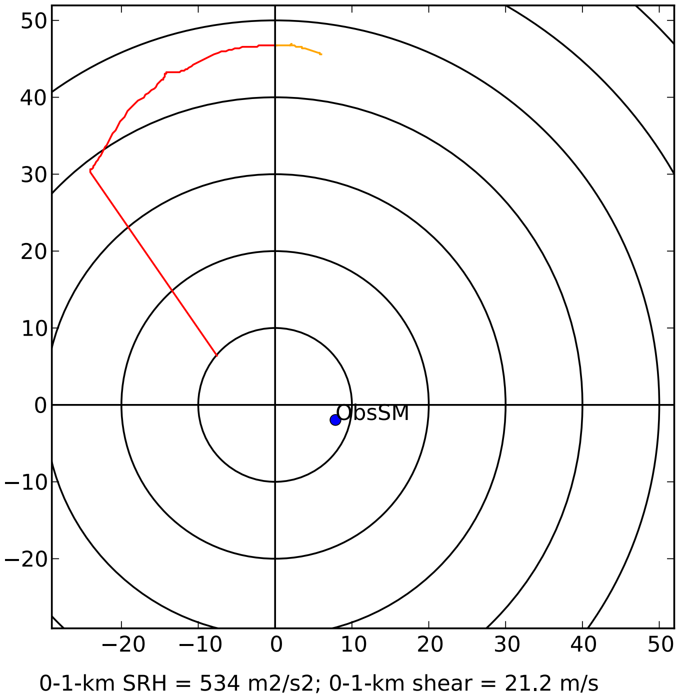

Fig. 27: 0003 UTC 16 May 2013 hodograph. Observed storm motion is noted here and in other hodographs where applicable.

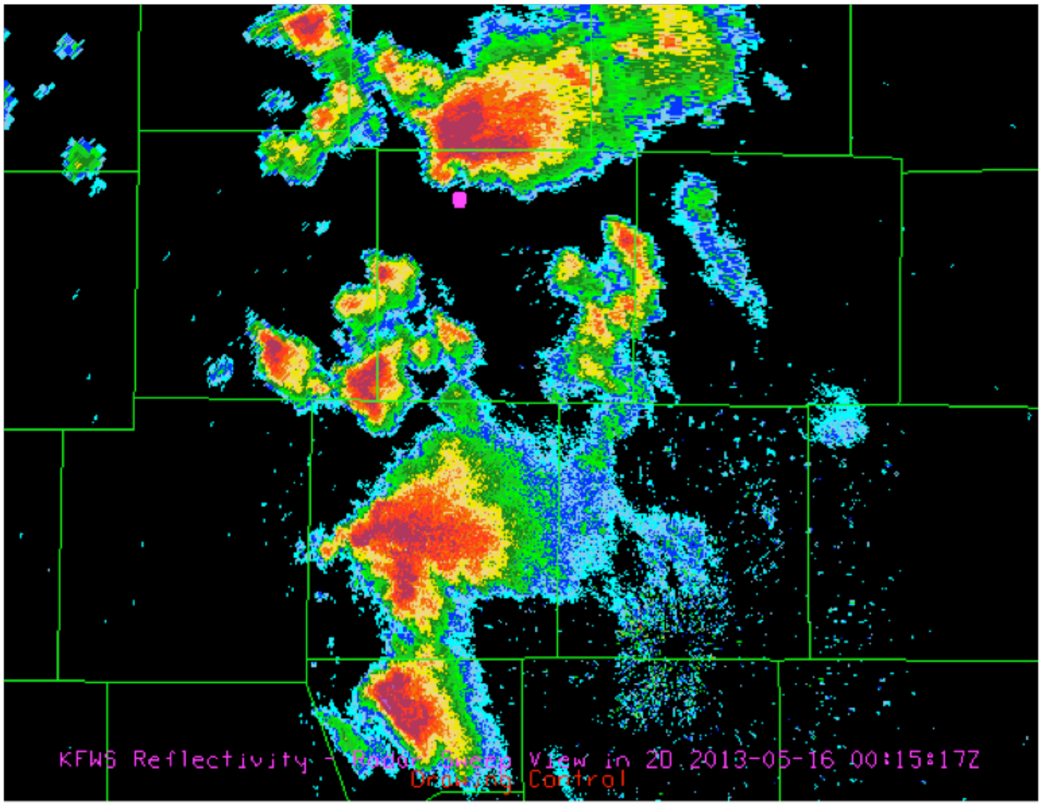

Fig. 28: Release point of 0017 UTC 16 May 2013 MPEX sounding, overlaid with KFWD WSR-88D radar reflectivity.

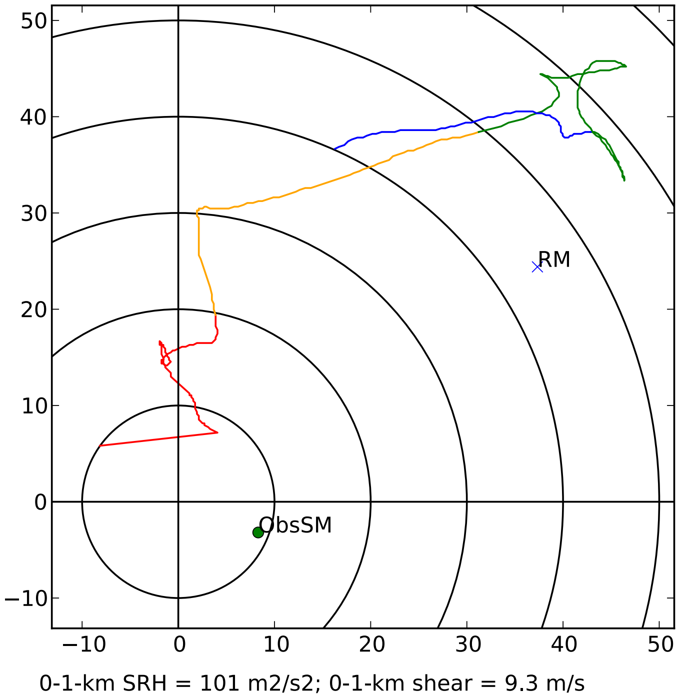

Fig. 29: 0017 UTC 16 May 2013 hodograph. Here and in all following hodographs where Bunkers rightward motion can be calculated, it is denoted as 'RM.' In addition to the hodograph sections described in Fig. 19, the green section extends from 3 to 6 km AGL, and the blue section extends from 6 to 8 km AGL.

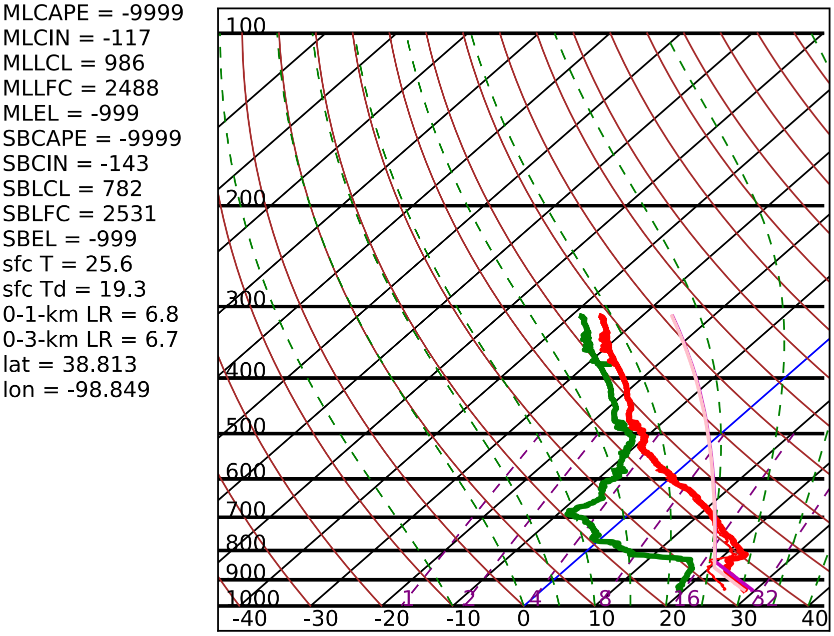

Fig. 30: Skew-*T* log-*p* diagram of 0000 UTC 19 May 2013 sounding.

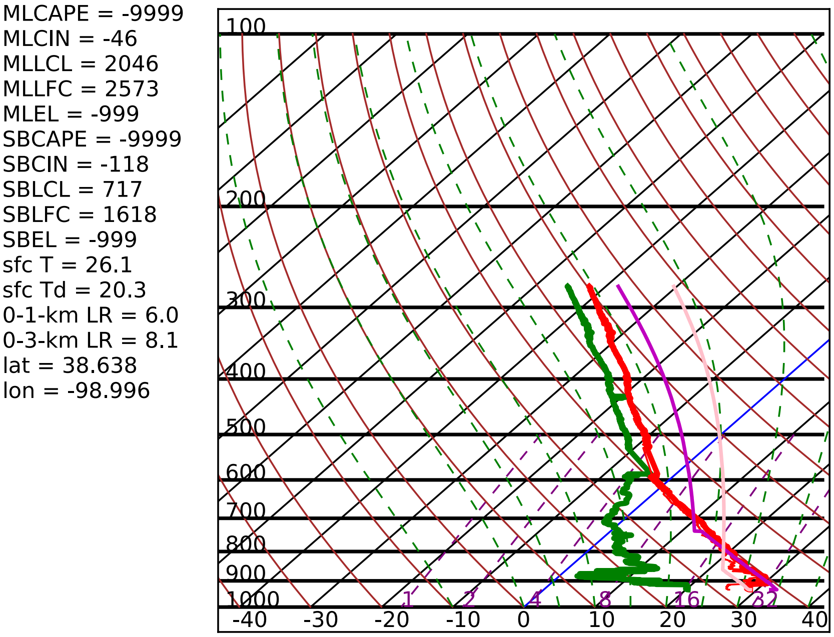

Fig. 31: Skew-*T* log-*p* diagram of 0001 UTC 19 May 2013 sounding.

MLCAPE = -9999
MLCIN = -12
MLLCL = -999
MLLFC = -999
MLEL = -999
SBCAPE = -9999
SBCIN = -257
SBLCL = 1816
SBLFC = 2588
SBEL = -999
sfc T = 27.2
sfc Td = 12.2
0-1-km LR = 6.1
lat = 38.826
lon = -98.848

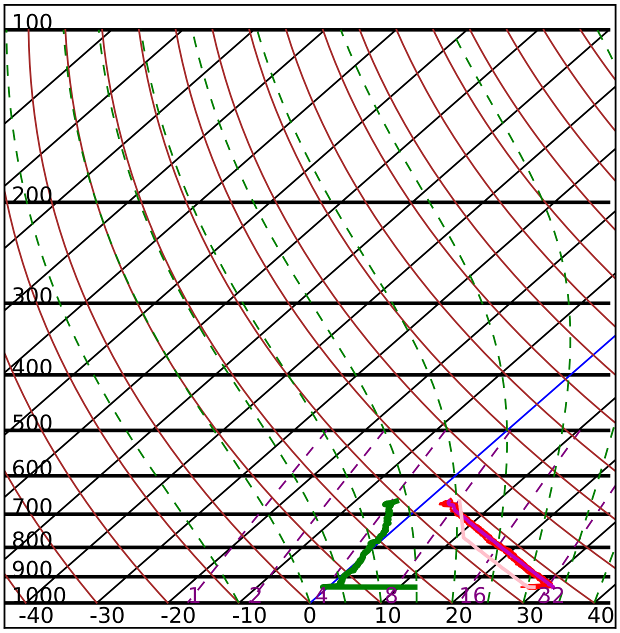

Fig. 32: Skew-*T* log-*p* diagram of 0041 UTC 19 May 2013 sounding.

MLCAPE = -9999
MLCIN = -44
MLLCL = 1115
MLLFC = 1843
MLEL = -999
SBCAPE = -9999
SBCIN = -28
SBLCL = 806
SBLFC = 1566
SBEL = -999
sfc T = 30.1
sfc Td = 23.6
0-1-km LR = 7.3
0-3-km LR = 7.9
lat = 35.300
lon = -98.260

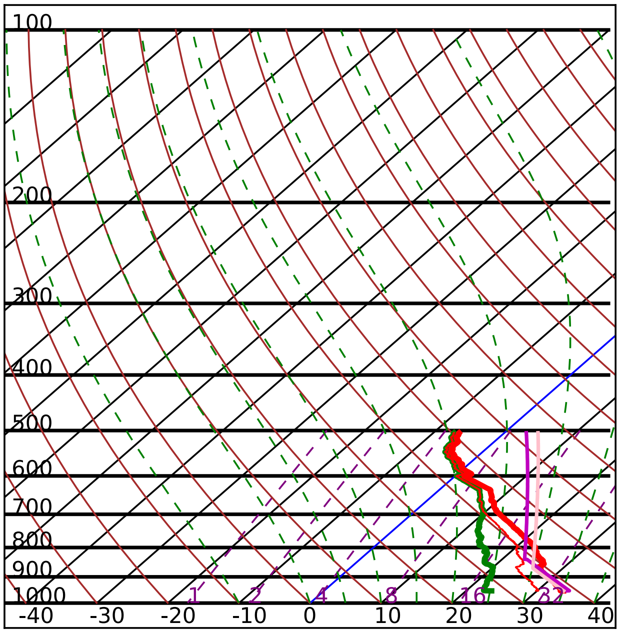

Fig. 33: Skew-*T* log-*p* diagram of 2241 UTC 31 May 2013 sounding.

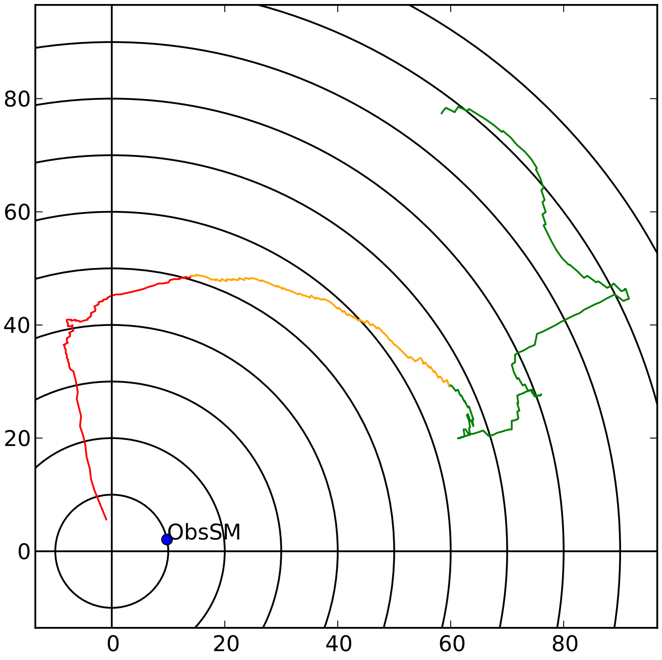

0-1-km SRH = 475 m2/s2; 0-1-km shear = 23.4 m/s

Fig. 34: Hodograph of 2241 UTC 31 May 2013 sounding.

MLCAPE = -9999
MLCIN = -56
MLLCL = 1079
MLLFC = 1832
MLEL = -999
SBCAPE = -9999
SBCIN = -14
SBLCL = 734
SBLFC = 1252
SBEL = -999
sfc T = 29.7
sfc Td = 23.9
0-1-km LR = 7.2
0-3-km LR = 8.1
lat = 35.333
lon = -98.096

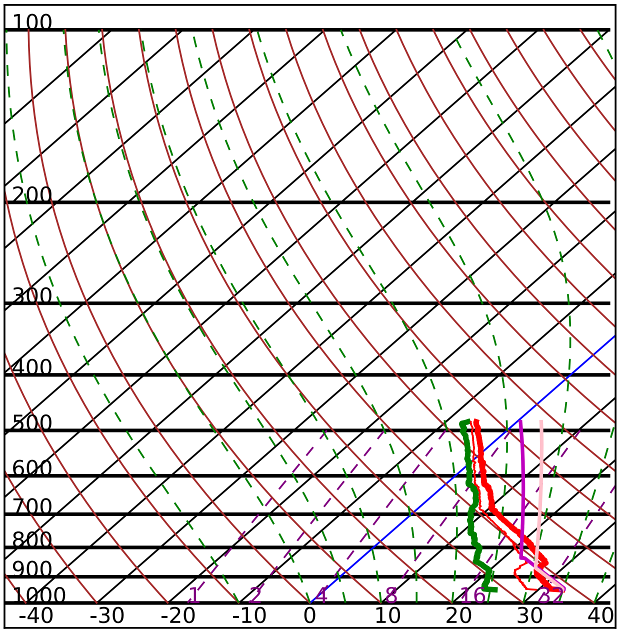

Fig. 35: Skew-*T* log-*p* diagram of 2300 UTC 31 May 2013 sounding.

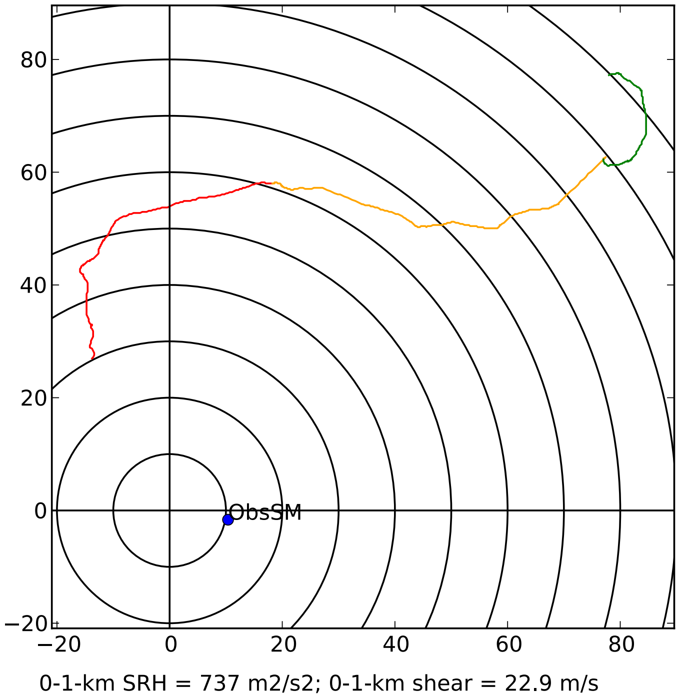

Fig. 36: Hodograph of 2300 UTC 31 May 2013 sounding.

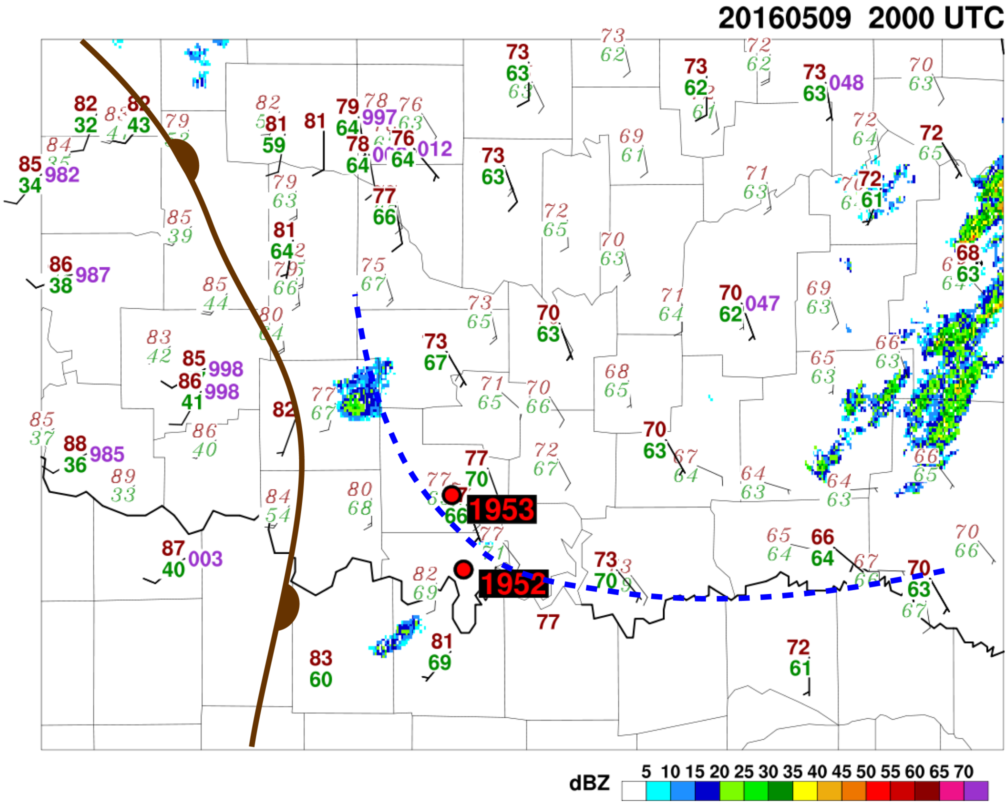

Fig. 37: Surface conditions preceding 9 May 2016 tornado event. Pre-storm Mini-MPEX sounding locations are marked.

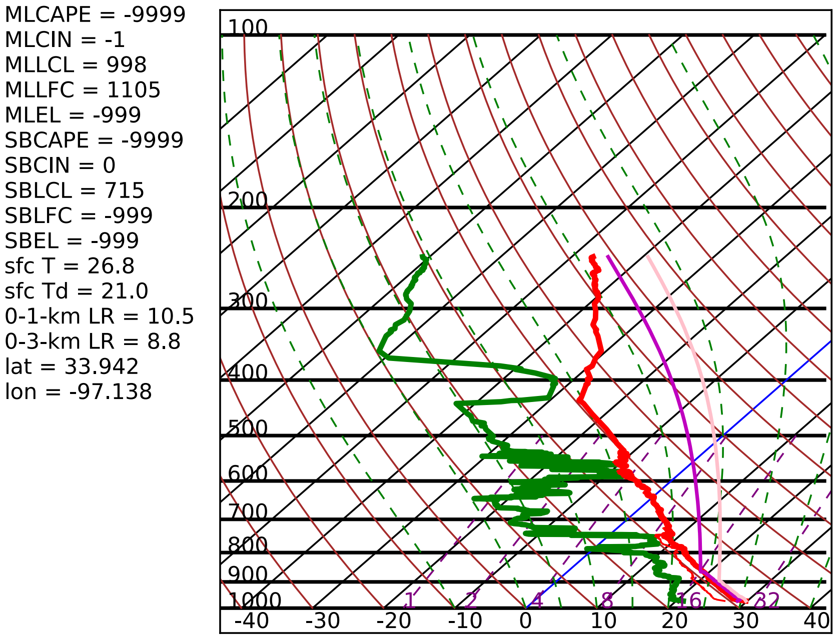
MLCAPE = -9999
MLCIN = -1
MLLCL = 998
MLLFC = 1105
MLEL = -999
SBCAPE = -9999
SBCIN = 0
SBLCL = 715
SBLFC = -999
SBEL = -999
sfc T = 26.8
sfc Td = 21.0
0-1-km LR = 10.5
0-3-km LR = 8.8
lat = 33.942
lon = -97.138

Fig. 38: Skew-*T* log-*p* diagram of 1952 UTC 9 May 2016 sounding.

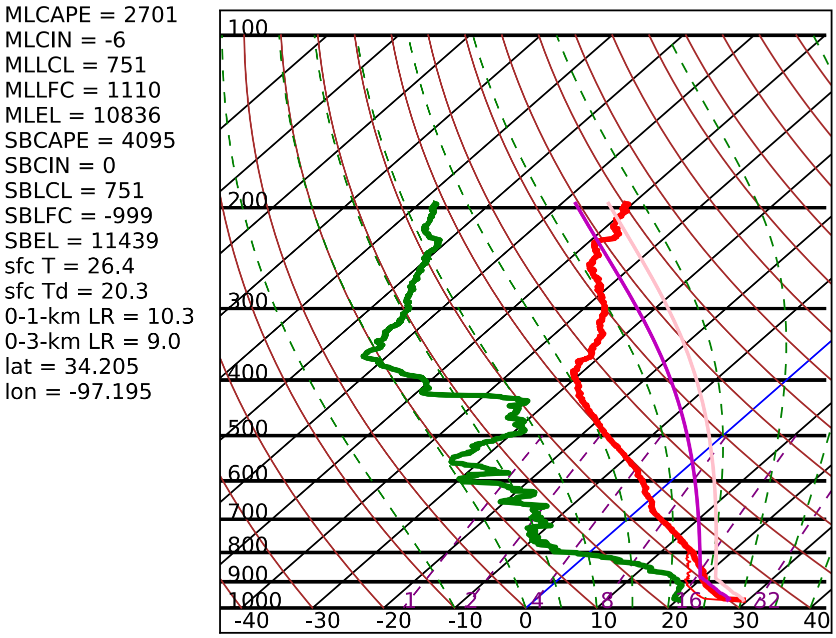

Fig. 39: Skew-*T* log-*p* diagram of 1953 UTC 9 May 2016 sounding.

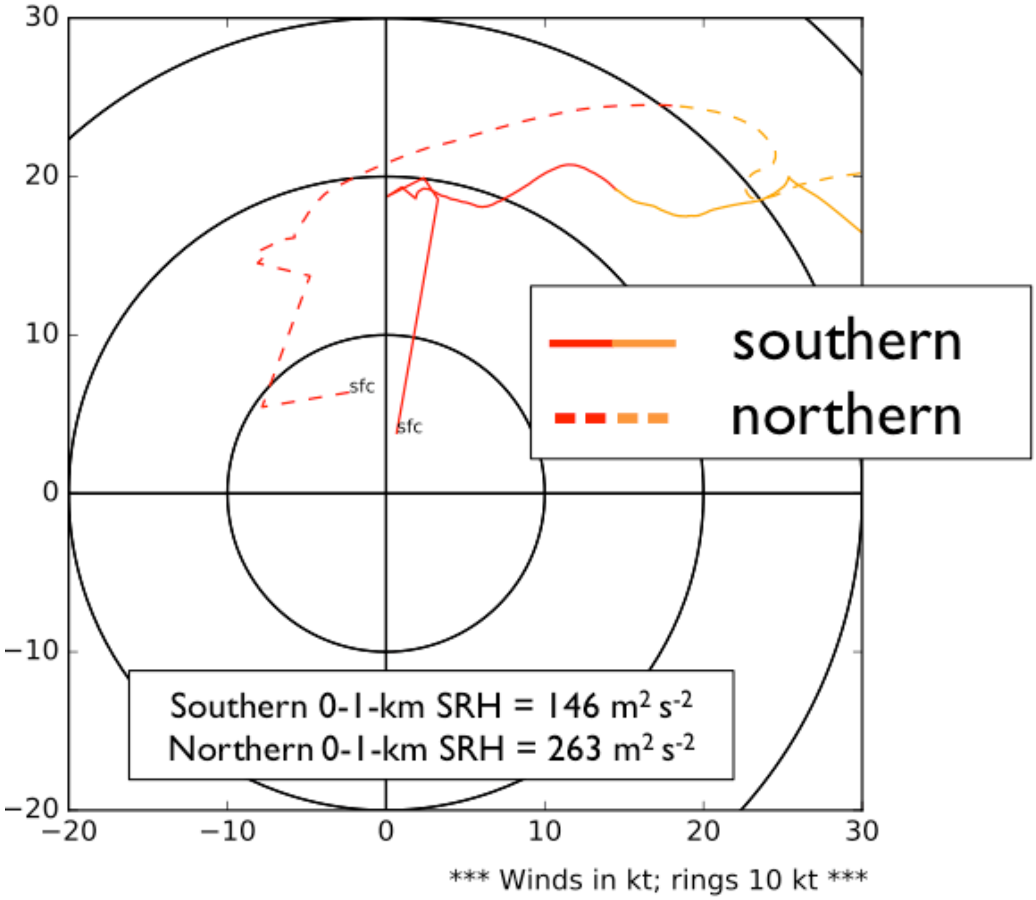

Fig. 40: Hodographs of 1952 and 1953 UTC 9 May 2016 soundings.

MLCAPE = -9999
MLCIN = -8
MLLCL = 959
MLLFC = 1248
MLEL = -999
SBCAPE = -9999
SBCIN = -7
SBLCL = 570
SBLFC = 863
SBEL = -999
sfc T = 24.7
sfc Td = 20.1
0-1-km LR = 8.2
0-3-km LR = 8.4
lat = 34.522
lon = -97.213

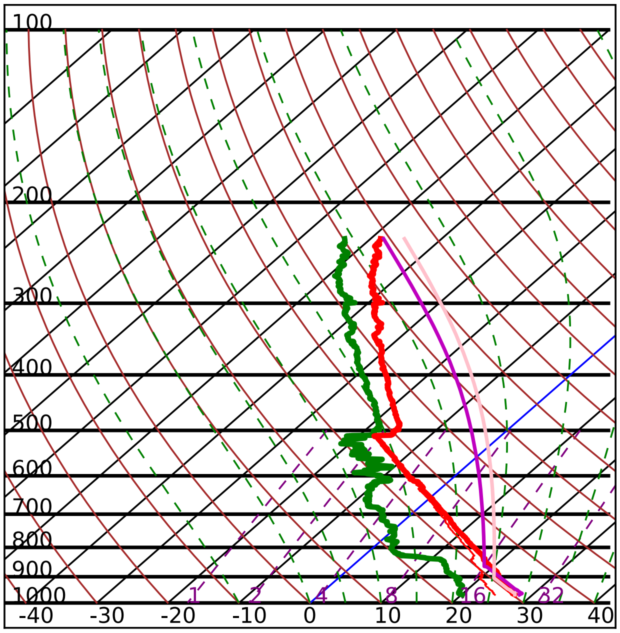

Fig. 41: Skew-*T* log-*p* diagram of 2046 UTC 9 May 2016 sounding.

MLCAPE = -9999
MLCIN = -1
MLLCL = 841
MLLFC = 961
MLEL = -999
SBCAPE = -9999
SBCIN = -2
SBLCL = 385
SBLFC = 567
SBEL = -999
sfc T = 24.5
sfc Td = 21.5
0-1-km LR = 8.6
0-3-km LR = 8.5
lat = 34.303
lon = -97.100

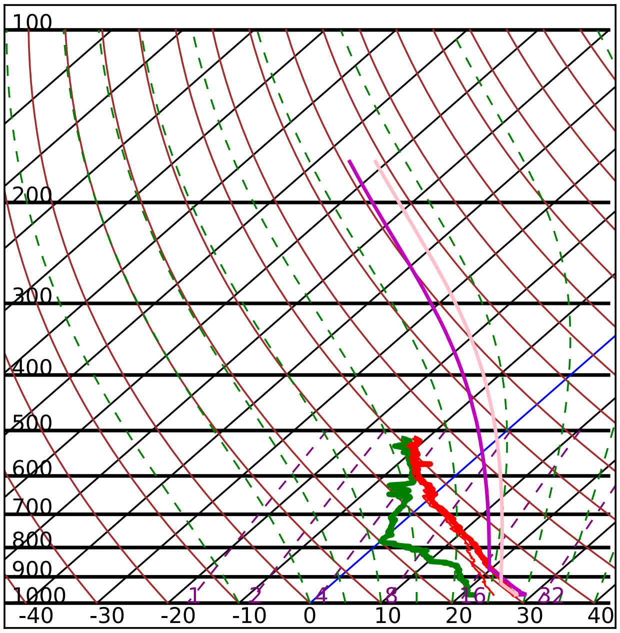

Fig. 42: Skew-*T* log-*p* diagram of 2052 UTC 9 May 2016 sounding.

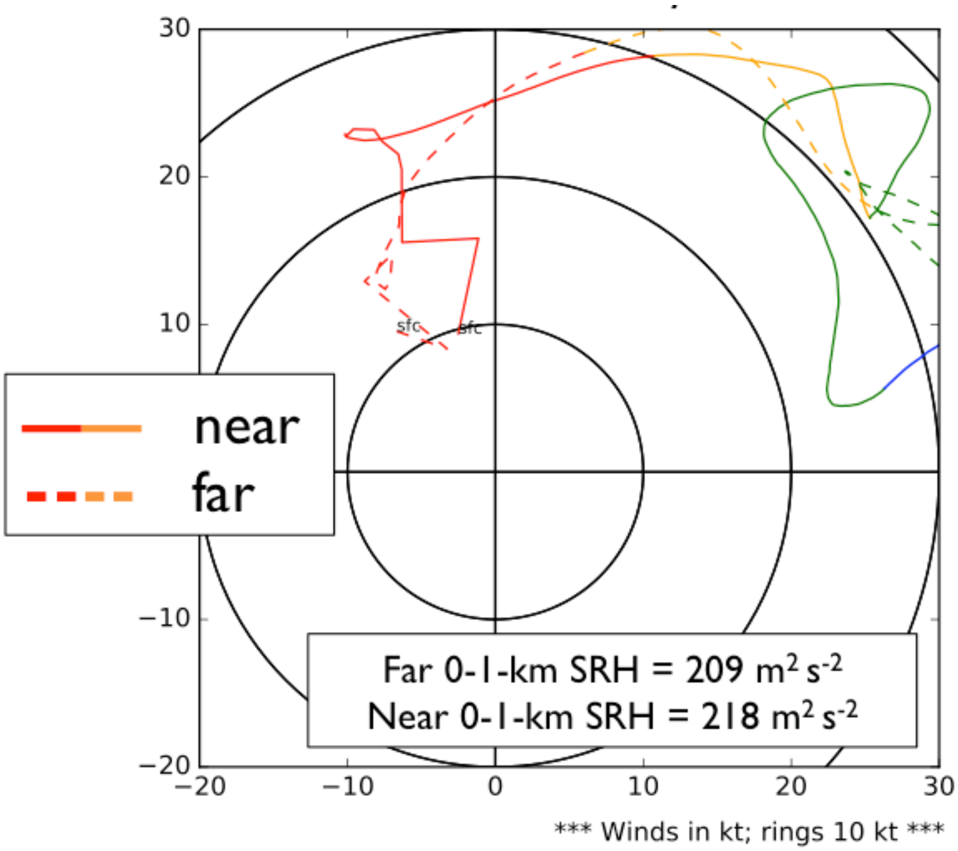

Fig. 43: Hodographs of 2046 and 2052 UTC 9 May 2016 soundings.

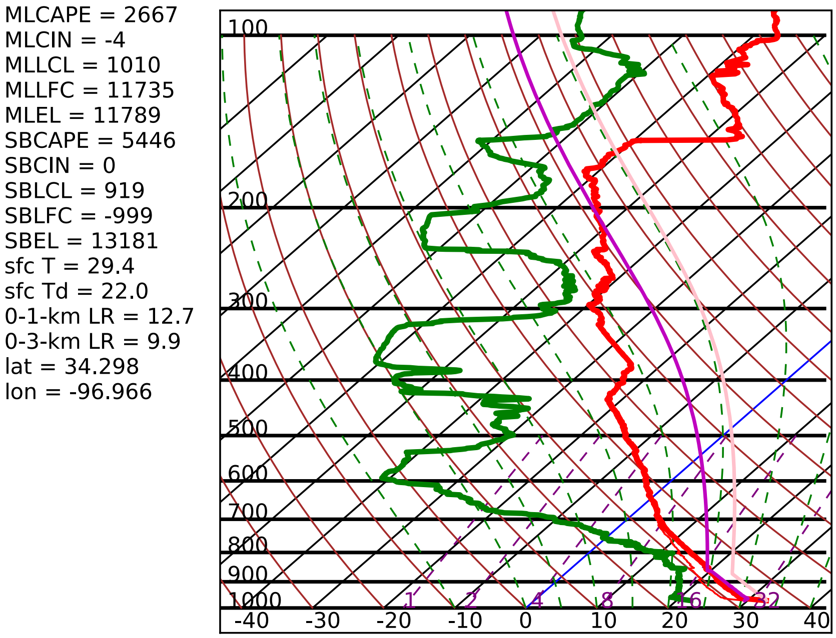

MLCAPE = 2667
MLCIN = -4
MLLCL = 1010
MLLFC = 11735
MLEL = 11789
SBCAPE = 5446
SBCIN = 0
SBLCL = 919
SBLFC = -999
SBEL = 13181
sfc T = 29.4
sfc Td = 22.0
0-1-km LR = 12.7
0-3-km LR = 9.9
lat = 34.298
lon = -96.966

Fig. 44: Skew-*T* log-*p* diagram of 2204 UTC 9 May 2016 sounding.

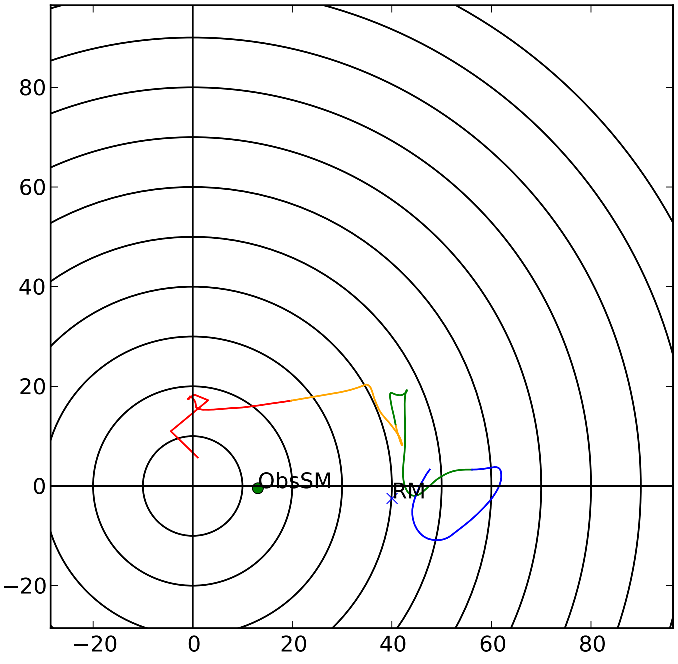

0-1-km SRH = 160 m2/s2; 0-1-km shear = 11.1 m/s

Fig. 45: Hodograph of 2204 UTC 9 May 2016 sounding.

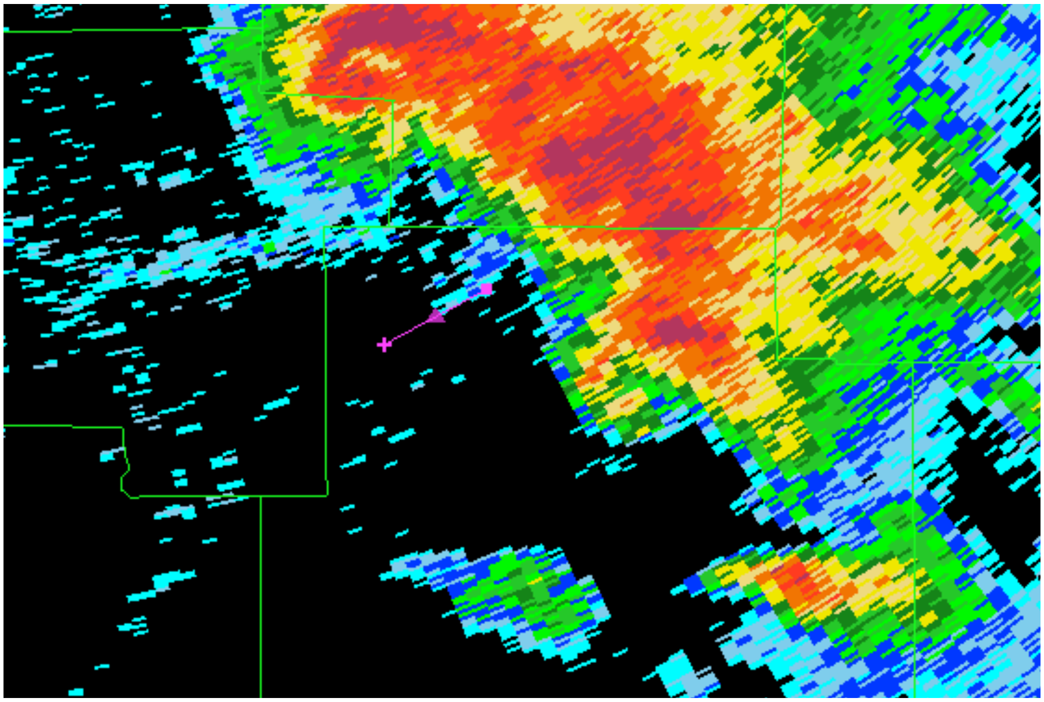

Fig. 46: Release point of 2204 UTC 9 May 2016 sounding, overlaid with KTLX WSR-88D radar reflectivity. Marker extends from release point to approximate location of incipient rear-flank tornado.

Fig. 47: Photograph of rear-flank tornado at ~2220 UTC 9 May 2016.

MLCAPE = 4143
MLCIN = -3
MLLCL = 1139
MLLFC = 1352
MLEL = 13103
SBCAPE = 5433
SBCIN = 0
SBLCL = 981
SBLFC = -999
SBEL = 13585
sfc T = 29.7
sfc Td = 21.9
0-1-km LR = 10.2
0-3-km LR = 8.0
lat = 34.566
lon = -99.771

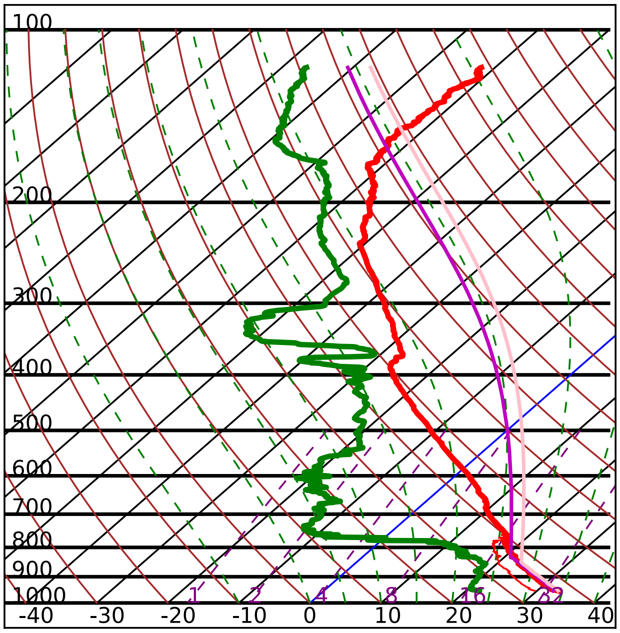

Fig. 48: Skew-*T* log-*p* diagram of 2131 UTC 23 May 2016 sounding.

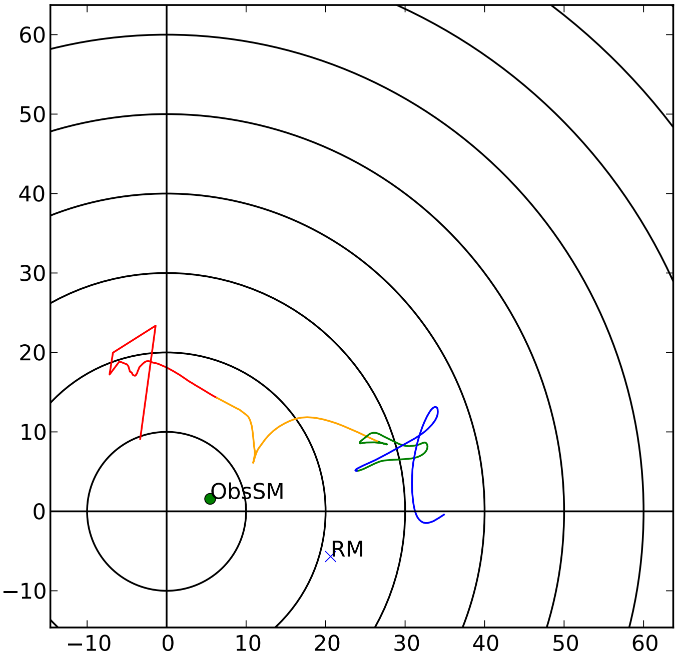

0-1-km SRH = 49 m2/s2; 0-1-km shear = 5.6 m/s

Fig. 49: Hodograph of 2131 UTC 23 May 2016 sounding.

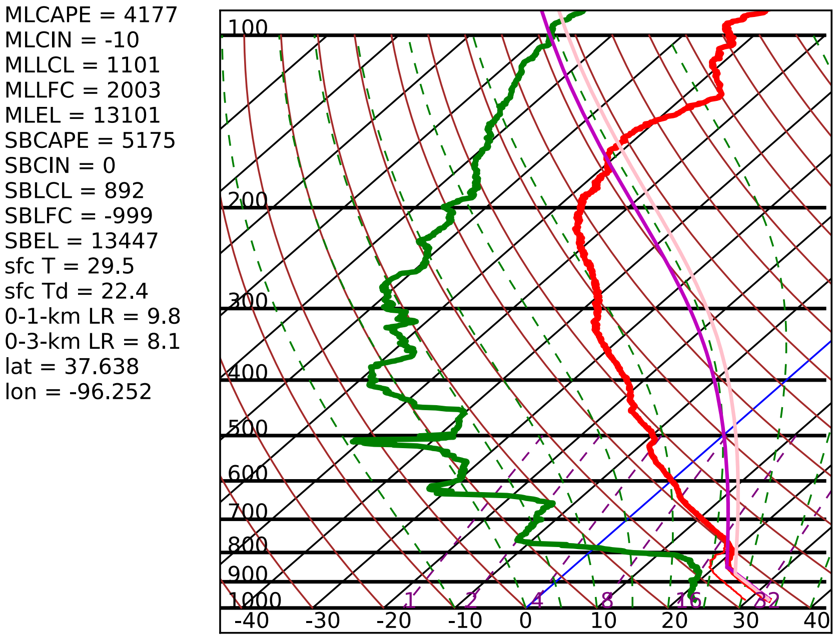

Fig. 50: Skew-*T* log-*p* diagram of 2332 UTC 25 May 2016 sounding.

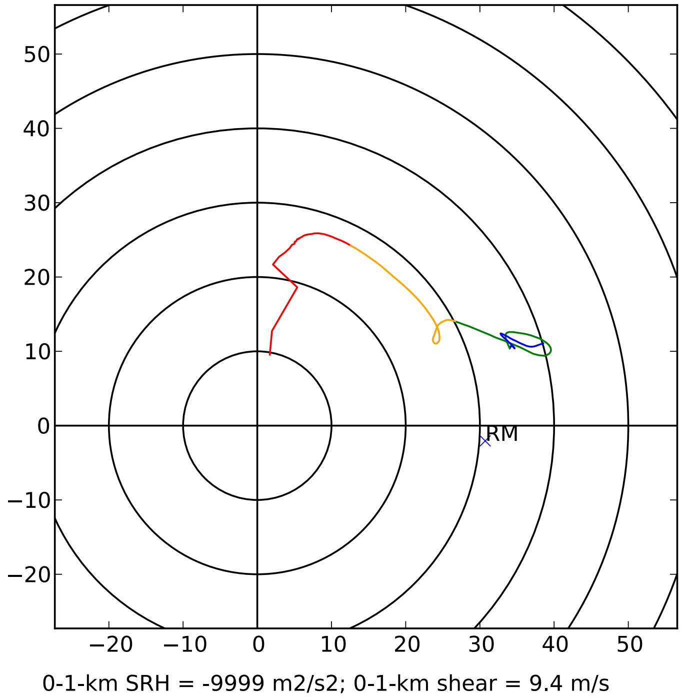

Fig. 51: Hodograph of 2332 UTC 25 May 2016 sounding.

Fig. 52: Photograph of 25 May 2016 storm in south-central Kansas.

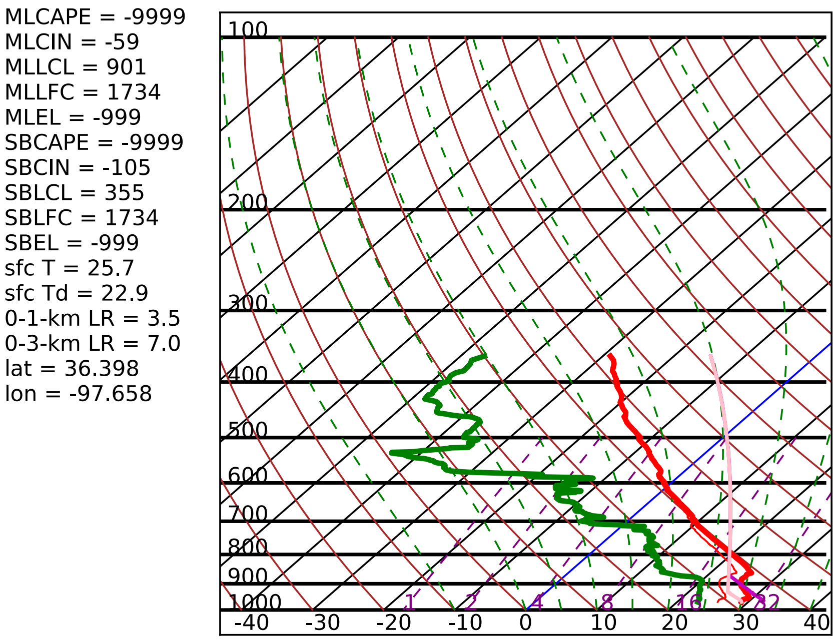

MLCAPE = -9999
MLCIN = -59
MLLCL = 901
MLLFC = 1734
MLEL = -999
SBCAPE = -9999
SBCIN = -105
SBLCL = 355
SBLFC = 1734
SBEL = -999
sfc T = 25.7
sfc Td = 22.9
0-1-km LR = 3.5
0-3-km LR = 7.0
lat = 36.398
lon = -97.658

Fig. 53: Skew-*T* log-*p* diagram of 0256 UTC 26 May 2016 near-field sounding.

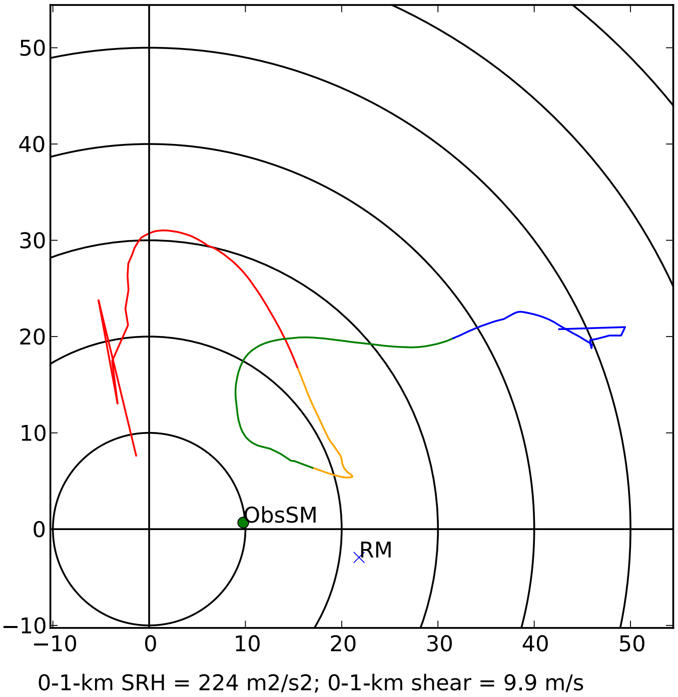

0-1-km SRH = 224 m2/s2; 0-1-km shear = 9.9 m/s

Fig. 54: Hodograph of 0256 UTC 26 May 2016 near-field sounding.